A Non-Stationary Subdivision Scheme for the Construction of Deformable Models with Sphere-Like Topology

Anaïs Badoual[a,*], Paola Novara[b], Lucia Romani[c], Daniel Schmitter[a], Michael Unser[a]

[a] *Biomedical Imaging Group, École polytechnique fédérale de Lausanne (EPFL), Lausanne, Switzerland*
[b] *Dipartimento di Scienza e Alta Tecnologia, Università dell'Insubria, Como, Italy*
[c] *Dipartimento di Matematica e Applicazioni, Università di Milano-Bicocca, Milano, Italy*

Abstract

We present an affine-invariant non-stationary subdivision scheme for the recursive refinement of any triangular mesh that is regular or has extraordinary vertices of valence 4. In particular, when applied to an arbitrary convex octahedron, it produces a G^1-continuous surface with a blob-like shape as the limit of the recursive subdivision process. In case of a regular octahedron, the subdivision process provides an accurate representation of ellipsoids. Our scheme allows us to easily construct a new interactive 3D deformable model for use in the delineation of biomedical images, which we illustrate by examples that deal with the characterization of 3D structures with sphere-like topology such as embryos, nuclei, or brains.

Keywords: Non-stationary subdivision; exponential-polynomial generation; extraordinary vertex; deformable model; delineation; biomedical imaging.

1. Introduction

An important challenge in biomedical imaging is the characterization of 3D structures. In a clinical context, the delineation of organs such as lungs and kidneys allows for better 3D visualization and, hence, facilitates preoperative steps. In a biological context, microscopic images often contain hundreds of cells for which an automatized or semi-automatized cell segmentation is necessary, because the manual delineation of each cell would otherwise be overly time consuming.
3D deformable models are powerful tools for the extraction of volumetric structures. They consist in flexible surfaces that are deformed from an initial user-provided configuration toward the boundary of the object to delineate. The deformation can be driven manually, by interactively modifying the parameters of the model, or automatically, by applying suitable energies [14, 27]. Currently, 3D deformable models are described either implicitly, by level sets [2], or explicitly, by meshes [8, 11] and parameterizations [25]. Therefore, the explicit definition of 3D deformable models can typically rely either on a discrete (mesh-based) or a continuous (parametric) representation. A good deformable model must fulfill two main requirements. First, it must depend on a small number of parameters (called control points), which limits the complexity of the deformation and improves robustness. Second, since we want to detect blob-like objects, it must reproduce or approximate ellipsoids.
In recent years, the trend in computer graphics has been to use subdivision surfaces as geometric tools for representation and modeling [10, 18]. A subdivision scheme consists in a refinement process that is recursively applied to an initial coarse polygonal mesh. Since, once infinitely refined, it provides a continuously defined

*Corresponding author
Email addresses: anais.badoual@epfl.ch (Anaïs Badoual), paola.novara@uninsubria.it (Paola Novara), lucia.romani@unimib.it (Lucia Romani), daniel.schmitter@epfl.ch (Daniel Schmitter), michael.unser@epfl.ch (Michael Unser)

surface, the set of the coarse mesh initial vertices, although discrete, is sufficient to fully describe the limit surface.

The goal pursued in this paper is to describe the surface of a 3D deformable model by the continuous limit surface obtained by applying a subdivision scheme to a suitable coarse mesh. The vertices of this initial coarse mesh are regarded as the control points of the deformable model. The idea of a subdivision-based deformable model offers the following advantages: i) the model can handle surfaces of arbitrary topological type; ii) easy and localized interactions can be achieved by simply modifying the control points; iii) the discrete nature of the scheme leads to an easy implementation.

In order to have few control points to manipulate, and as the number of mesh vertices increases geometrically at each subdivision step, we want a simple shape as initial mesh. Since we focus our attention on the construction of 3D deformable models for the characterization of structures with sphere-like topology, we choose as initial mesh a 2-manifold triangular mesh with genus 0. In particular, among the Platonic solids having triangular faces and a low number of vertices, we choose the octahedron. It is the one that has a vertex valence closest to the regular valence 6. (The icosahedron is discarded for its high number of vertices and the octahedron is preferred to the tetrahedron since it has vertex valence 4 rather than 3.)

To the best of our knowledge, the only subdivision methods that allow one to construct a good approximation of the unit sphere, starting from a 2-manifold polygon mesh with arbitrary connectivity, are the polar method proposed in [15] and improvements thereof proposed in [22]. These methods can be used on polar meshes, which are meshes with sphere-like topology described by triangles in the vicinity of extraordinary vertices (*i.e.*, internal vertices with a number of incident edges that differ from the regular valence), and made of quadrilaterals elsewhere. However, the extraordinary vertices contained in the polar meshes are not allowed to have a valence smaller than 6. As a consequence, the methods proposed in [15] and [22] cannot be applied to initial triangular meshes defined by six vertices of valence 4, as is the case with the regular octahedron.

A subdivision scheme that is able to handle a regular octahedron is Loop's scheme. It is an approximating subdivision scheme for triangular meshes developed by Charles Loop in 1987 [19]. At each step of the subdivision process, it refines each triangle of a given mesh into four subtriangles, obtained by inserting one new vertex in correspondence to each edge midpoint and to each existing vertex [1, 19]. If applied to a 2-manifold triangle mesh with arbitrary connectivity, it generates a limit surface of arbitrary topology that is C^2-continuous everywhere, except at extraordinary vertices where the regularity is only C^1. Thus, by applying Loop's scheme to a regular octahedron, we get a limit surface that is globally C^1-continuous. However, as we show in Section 3.1.4, it provides a bad approximation of the unit sphere because the stencil used by Loop's scheme to insert a new vertex in correspondence to an edge midpoint is too small to take into account the desired geometry and does not adapt to the refinement step.

In this paper, we resolve this issue by proposing a new non-stationary (or level-dependent) subdivision scheme. Like Loop's scheme, it belongs to the class of *primal* subdivision schemes [1, 23] since, at each step of the refinement process, a finer mesh is created by splitting the faces of the coarse mesh. However, we use a level-dependent vertex-point stencil and a much larger (and also level-dependent) edge-point stencil. These modified rules for inserting new vertices fulfill the following properties:

1. affine invariance, which ensures that the limit surface is described independently of its location and orientation;
2. applicability to an initial mesh with very few control points;
3. G^1-continuity of the limit surface;
4. accurate representation of ellipsoids;
5. friendly user interactions whenever some manual editing of the model is desired.

1.1. Organization of the Article

In Section 2, we present our new non-stationary subdivision scheme. Then, in Section 3, we analyze its main properties. Finally, in Section 4, we illustrate how it can be effectively exploited to construct deformable models with sphere-like topology. We also provide application examples in real volumetric biomedical images. Conclusions are drawn in Section 5.

2. BLOB: A Butterfly-Loop Optimal Blending Non-Stationary Subdivision Scheme

In this section, we present our new non-stationary subdivision scheme for the construction of 3D deformable models with sphere-like topology.

2.1. Notation and Vocabulary

In this paper we focus on 2-manifold triangular meshes with genus 0 [12], where each vertex is the meeting point of an arbitrary number n ($n \geq 3$) of triangles. The value assumed by n is called the valence of the vertex. Vertices of a triangular mesh are called regular when they have valence $n = 6$ and extraordinary otherwise. Let $\mathcal{M}^{(0)}$ denote an initial 2-manifold triangular mesh. Then, the finer resolution mesh $\mathcal{M}^{(k)}$, $k \in \mathbb{N}^* := \mathbb{N} \setminus \{0\}$, is obtained by means of the recursive application of the subdivision operators $\{\mathcal{S}_n,\, n = 0, \ldots, k-1\}$ that identify the non-stationary subdivision scheme, as

$$\mathcal{M}^{(k)} = \mathcal{S}_{k-1}\mathcal{S}_{k-2}\cdots\mathcal{S}_0\mathcal{M}^{(0)}. \tag{2.1}$$

Since the subdivision operators are defined locally, in the remainder of this paper we denote by $\mathcal{R}^{(0)}$ and $\mathcal{E}^{(0)}$ the submeshes of $\mathcal{M}^{(0)}$ that determine the behavior of the limit surface on the one-ring of a regular and of an extraordinary vertex, respectively. The submesh $\mathcal{R}^{(0)}$ ($\mathcal{E}^{(0)}$, respectively) is also called the neighborhood of a regular (extraordinary, respectively) vertex.
In Sections 2.2 and 2.3, we describe how the subdivision operators perform in $\mathcal{R}^{(0)}$ and $\mathcal{E}^{(0)}$, respectively.

2.2. Regular Subdivision Rules

We denote by $\mathbf{q}^{(0)} = \{\mathrm{q}_{\boldsymbol{\alpha}}^{(0)},\, \boldsymbol{\alpha} \in \mathbb{Z}^2\}$ the set of vertices in the submesh $\mathcal{R}^{(0)}$. Following the standard notation of [5], at each level $k \in \mathbb{N}$, the action of a non-stationary scheme on $\mathcal{R}^{(0)}$ is described by the refinement rules

$$\mathrm{q}_{\boldsymbol{\alpha}}^{(k+1)} = \sum_{\boldsymbol{\beta}\in\mathbb{Z}^2} \mathrm{a}_{\boldsymbol{\alpha}-2\boldsymbol{\beta}}^{(k)}\, \mathrm{q}_{\boldsymbol{\beta}}^{(k)}, \quad \boldsymbol{\alpha} \in \mathbb{Z}^2, \tag{2.2}$$

which generate the refined data sequence $\mathbf{q}^{(k+1)} = \{\mathrm{q}_{\boldsymbol{\alpha}}^{(k+1)},\, \boldsymbol{\alpha} \in \mathbb{Z}^2\}$ starting from the coarser data sequence $\mathbf{q}^{(k)} = \{\mathrm{q}_{\boldsymbol{\alpha}}^{(k)},\, \boldsymbol{\alpha} \in \mathbb{Z}^2\}$. The coefficients in (2.2), which are assumed to be finitely many, can be conveniently collected in the kth-level *subdivision mask*

$$\mathbf{a}^{(k)} = \{\mathrm{a}_{\boldsymbol{\alpha}}^{(k)},\, \boldsymbol{\alpha} \in \mathbb{Z}^2\}$$

or incorporated in the kth-level *subdivision symbol*

$$a_*^{(k)}(\boldsymbol{z}) = \sum_{\boldsymbol{\alpha}\in\mathbb{Z}^2} \mathrm{a}_{\boldsymbol{\alpha}}^{(k)} \boldsymbol{z}^{\boldsymbol{\alpha}}, \quad \boldsymbol{z} \in (\mathbb{C}\setminus\{0\})^2.$$

For our specific scheme, the kth-level subdivision mask is of the form

$$\mathbf{a}^{(k)} = \{\mathrm{a}_{\alpha_1,\alpha_2}^{(k)},\, -3 \leq \alpha_1, \alpha_2 \leq 3\} = \begin{pmatrix} 0 & 0 & 0 & e^{(k)} & c^{(k)} & c^{(k)} & e^{(k)} \\ 0 & 0 & c^{(k)} & b^{(k)} & d^{(k)} & b^{(k)} & c^{(k)} \\ 0 & c^{(k)} & d^{(k)} & f^{(k)} & f^{(k)} & d^{(k)} & c^{(k)} \\ e^{(k)} & b^{(k)} & f^{(k)} & a^{(k)} & f^{(k)} & b^{(k)} & e^{(k)} \\ c^{(k)} & d^{(k)} & f^{(k)} & f^{(k)} & d^{(k)} & c^{(k)} & 0 \\ c^{(k)} & b^{(k)} & d^{(k)} & b^{(k)} & c^{(k)} & 0 & 0 \\ e^{(k)} & c^{(k)} & c^{(k)} & e^{(k)} & 0 & 0 & 0 \end{pmatrix}, \tag{2.3}$$

where the non-zero entries are

$$\begin{aligned} a^{(k)} &= \tfrac{4(v^{(k)})^2+2v^{(k)}+1}{4(v^{(k)}+1)^2}, & b^{(k)} &= \tfrac{2v^{(k)}+1}{8(v^{(k)}+1)^2}, & c^{(k)} &= \tfrac{2v^{(k)}+1}{16(v^{(k)}+1)^3}, \\ d^{(k)} &= \tfrac{(2v^{(k)}+1)^2}{8(v^{(k)}+1)^3}, & e^{(k)} &= \tfrac{1}{16(v^{(k)}+1)^3}, & f^{(k)} &= \tfrac{(2v^{(k)}+1)(4(v^{(k)})^2+6v^{(k)}+3)}{16(v^{(k)}+1)^3}, \end{aligned}$$

with

$$v^{(k)} = \frac{1}{2}\left(\mathrm{e}^{\,\mathrm{i}\frac{\lambda}{2^{(k+1)}}} + \mathrm{e}^{\,-\mathrm{i}\frac{\lambda}{2^{(k+1)}}}\right), \qquad \lambda \in [0,\pi) \cup \mathrm{i}(0, 2\mathrm{acosh}(500)). \tag{2.4}$$

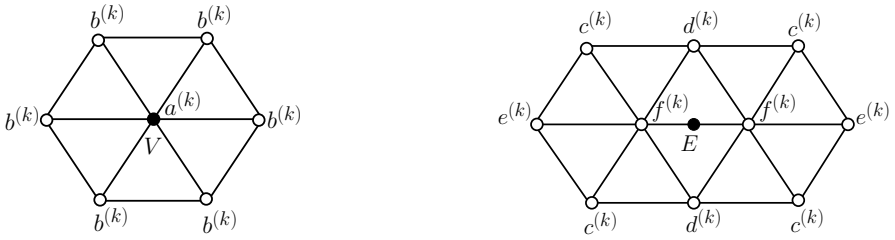

(a) Vertex-point stencil.

(b) Edge-point stencil.

Figure 1: Stencils for vertex-point (a) and edge-point (b) rules of the BLOB scheme in the regular regions of the mesh.

Remark 2.1. *The parameter λ influences the final shape of the limit surface. Since*

$$v^{(0)} = \frac{1}{2}\left(\mathrm{e}^{\mathrm{i}\frac{\lambda}{2}} + \mathrm{e}^{-\mathrm{i}\frac{\lambda}{2}}\right) = \begin{cases} \cos\left(\frac{\lambda}{2}\right) \in (0,1], & \lambda \in [0,\pi) \\ \cosh\left(\frac{Im(\lambda)}{2}\right) \in (1,500), & \lambda \in \mathrm{i}(0, 2\mathrm{acosh}(500)), \end{cases}$$

we can also assume $v^{(0)} \in (0, 500)$ to be the free parameter that specifies the shape of the surface we get in the limit.

The kth-level symbol associated to the subdivision mask in (2.3), written in terms of $v^{(k)}$, is thus

$$a_*^{(k)}(z_1, z_2) = \frac{(1+z_1)\,(1+z_2)\,(1+z_1z_2)\,(z_1^2 + 2v^{(k)}z_1 + 1)\,(z_2^2 + 2v^{(k)}z_2 + 1)\,(z_1^2z_2^2 + 2v^{(k)}z_1z_2 + 1)}{16(v^{(k)}+1)^3 z_1^3 z_2^3}. \quad (2.5)$$

For the mask coefficients in (2.3), the refinement rules in (2.2) give rise to the vertex-point and edge-point stencils illustrated in Figure 1, where local linear combinations of vertices are suggested graphically. The coarser mesh is used to create a new vertex in correspondence to either an old vertex or an old edge. Since the vertex-point rule has the same size and structure as the vertex-point rule of Loop's subdivision scheme [19], and since the size and structure of the edge-point rule are the same as those of the modified Butterfly scheme [31], the new scheme is named the Butterfly-Loop Optimal Blending (BLOB) subdivision scheme.

2.3. Extraordinary Subdivision Rules

We allow the starting mesh to contain extraordinary vertices of valence 4. In fact, we are interested in applying the BLOB scheme to an initial mesh given by an octahedron, which is a polyhedron made of eight triangular faces and six vertices that all have valence 4. The vertex-point stencil for an old vertex of valence 4 and the edge-point stencil for an old edge, where one or both endpoints are extraordinary vertices of valence 4, are illustrated in Figure 2. The rule to create our edge point with two extreme vertices of valence 4 (Figure 2 (b)) is only used in the first step of the subdivision process. In the subsequent steps, the extraordinary vertices are isolated; thus, the regular rule (Figure 1 (b)) and the rule for extreme vertices with different valences (Figure 2 (c)) are used. In addition, the rule for the computation of the vertex-point of valence 4 (Figure 2 (a)) is used six times in each subdivision step since the octahedron has six vertices of valence 4 and they are kept throughout the whole subdivision process.
Denoting by $\mathbf{p}^{(0)}$ the vector that collects the vertices of the submesh $\mathcal{E}^{(0)}$, we describe the action of the BLOB scheme in the vicinity of an extraordinary vertex of valence 4 by the kth-level equation $\mathbf{p}^{(k+1)} = \tilde{\mathbf{S}}_k \mathbf{p}^{(k)}$,

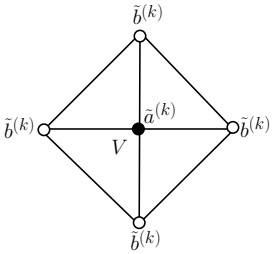

(a) Vertex-point rule for a vertex of valence 4.

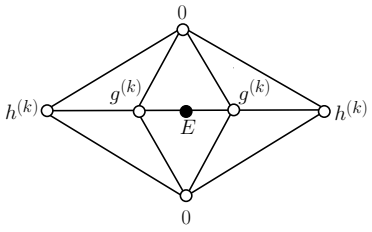

(b) Edge-point rule for an edge with two end-point vertices of valence 4. Here, $g^{(k)} = \frac{(2v^{(k)}+3)(2v^{(k)}+1)}{8(v^{(k)}+1)^2}$ and $h^{(k)} = \frac{1}{8(v^{(k)}+1)^2}$, with $k = 1$.

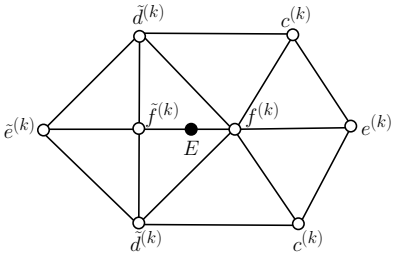

(c) Edge-point rule for an edge with one end-point vertex of valence 4 and the other of valence 6.

Figure 2: Stencils for vertex-point and edge-point rules involving extraordinary vertices of valence 4.

$k \in \mathbb{N}$ (see again [5]). The matrix $\tilde{\mathbf{S}}_k$ is the kth-level subdivision matrix, and for all $k > 1$, is of the form

$$\tilde{\mathbf{S}}_k = \left[\begin{array}{c|cccc} \tilde{a}^{(k)} & (\mathbf{r}^{(k)})^T & (\mathbf{r}^{(k)})^T & (\mathbf{r}^{(k)})^T & (\mathbf{r}^{(k)})^T \\ \hline \mathbf{s}^{(k)} & \mathbf{M}_0^{(k)} & \mathbf{M}_1^{(k)} & \mathbf{M}_2^{(k)} & \mathbf{M}_3^{(k)} \\ \mathbf{s}^{(k)} & \mathbf{M}_3^{(k)} & \mathbf{M}_0^{(k)} & \mathbf{M}_1^{(k)} & \mathbf{M}_2^{(k)} \\ \mathbf{s}^{(k)} & \mathbf{M}_2^{(k)} & \mathbf{M}_3^{(k)} & \mathbf{M}_0^{(k)} & \mathbf{M}_1^{(k)} \\ \mathbf{s}^{(k)} & \mathbf{M}_1^{(k)} & \mathbf{M}_2^{(k)} & \mathbf{M}_3^{(k)} & \mathbf{M}_0^{(k)} \end{array}\right], \tag{2.6}$$

where

$$\mathbf{M}_0^{(k)} = \begin{pmatrix} f^{(k)} & e^{(k)} & c^{(k)} \\ a^{(k)} & b^{(k)} & b^{(k)} \\ f^{(k)} & c^{(k)} & d^{(k)} \end{pmatrix}, \ \mathbf{M}_1^{(k)} = \begin{pmatrix} \tilde{d}^{(k)} & 0 & 0 \\ b^{(k)} & 0 & 0 \\ f^{(k)} & c^{(k)} & e^{(k)} \end{pmatrix}, \ \mathbf{M}_2^{(k)} = \begin{pmatrix} \tilde{e}^{(k)} & 0 & 0 \\ 0 & 0 & 0 \\ c^{(k)} & 0 & 0 \end{pmatrix}, \ \mathbf{M}_3^{(k)} = \begin{pmatrix} \tilde{d}^{(k)} & 0 & c^{(k)} \\ b^{(k)} & 0 & b^{(k)} \\ c^{(k)} & 0 & e^{(k)} \end{pmatrix},$$

$$\tilde{d}^{(k)} = \frac{16(v^{(k)})^2 + 18v^{(k)} + 5}{32(v^{(k)}+1)^3}, \qquad \tilde{e}^{(k)} = \frac{2v^{(k)}+5}{64(v^{(k)}+1)^3}$$

and

$$\tilde{a}^{(k)} = \frac{45(v^{(k)})^2 + 18v^{(k)} + 1}{48(v^{(k)}+1)^2}, \qquad \mathbf{r}^{(k)} = (\tilde{b}^{(k)}, 0, 0)^T, \qquad \mathbf{s}^{(k)} = (\tilde{f}^{(k)}, b^{(k)}, d^{(k)})^T,$$

with

$$\tilde{b}^{(k)} = \frac{3(v^{(k)})^2 + 78v^{(k)} + 47}{192(v^{(k)}+1)^2}, \quad \tilde{f}^{(k)} = \frac{32(v^{(k)})^3 + 64(v^{(k)})^2 + 54v^{(k)} + 15}{64(v^{(k)}+1)^3}.$$

Remark 2.2. *The coefficients $g^{(k)}$ and $h^{(k)}$ in Figure 2 (b) do not appear in the subdivision matrix* (2.6) *since the corresponding stencil is used only in the first step of the refinement process. The explicit form of the subdivision matrix $\tilde{\mathbf{S}}_k$ is given only for levels $k > 1$.*

3. Properties of the BLOB Scheme

In this section, we analyse the main properties of the BLOB scheme, including its capability of generating/reproducing bivariate exponential polynomials or blob-like shapes, affine invariance, convergence, and smoothness.

3.1. Generation and Reproduction Properties

Non-stationary subdivision schemes have become popular due to their capability to reproduce conic sections or surfaces of revolution, which appear very often in geometric modeling, isogeometric analysis, or biomedical imaging.

3.1.1. Generation of Exact Ellipsoids from a Regular Triangular Mesh with Poles

Proposition 3.1. *In the submesh $\mathcal{R}^{(0)}$, the BLOB subdivision scheme generates exponential polynomials from the space $EP_{(\Gamma_1,\Theta)}$, with $\Gamma_1 = \{(\gamma_1,\gamma_2) \in \mathbb{N}^2 : 0 \le \gamma_1+\gamma_2 \le 1\}$, $\Theta = \{(0,0),(\pm\lambda,0),(0,\pm\lambda),(\pm\lambda,\pm\lambda)\}$, $\lambda \in (0,\pi) \cup \mathrm{i}(0,2\mathrm{acosh}(500))$; that is,*

$$\mathrm{span}\big\{1,\, x,\, y,\, \mathrm{e}^{\pm\lambda x},\, \mathrm{e}^{\pm\lambda y},\, x\,\mathrm{e}^{\pm\lambda x},\, y\,\mathrm{e}^{\pm\lambda y}, x\,\mathrm{e}^{\pm\lambda x},\, y\,\mathrm{e}^{\pm\lambda x}, \mathrm{e}^{\pm\lambda(x+y)},\, \mathrm{e}^{\pm\lambda(x-y)},\, x\,\mathrm{e}^{\pm\lambda(x-y)},\, y\,\mathrm{e}^{\pm\lambda(x-y)}\big\}. \tag{3.1}$$

In particular, it reproduces linear polynomials from the space $\Pi_1^2 = \mathrm{span}\{1,\, x,\, y\}$ with respect to the parameterization $\{\mathbf{T}^{(k)}, k \in \mathbb{N}\}$, $\mathbf{T}^{(k)} = \{\mathbf{t}_{\boldsymbol{\alpha}}^{(k)} = \frac{\boldsymbol{\alpha}}{2^k}, \boldsymbol{\alpha} \in \mathbb{Z}^2\}$.

The proof of Proposition 3.1 is given in Appendix A. This gives the BLOB scheme the ability to generate exact ellipsoids, starting from a regular triangular mesh. To build an exact ellipsoid (Figure 4 (b)), we need to apply the regular rules shown in Figure 1 to the initial control mesh $\mathbf{q}^{(0)} = \{\phi(\mathbf{t}_{\boldsymbol{\alpha}}^{(0)}), \boldsymbol{\alpha} \in \mathbb{Z}^2\}$, where ϕ also denotes an ellipsoid, and select $\lambda \in (0,\pi)$ accordingly. Since we require the initial control mesh $\mathbf{q}^{(0)}$ to be regular (*i.e.*, made of vertices of valence 6), we apply the refinement process to an initial mesh described by the twenty-eight vertices of coordinates

$$[(\mathbf{q}^{(0)})_1]_{i,j} = \cos(s_{i-1})\cos(t_{j-1}), \qquad [(\mathbf{q}^{(0)})_2]_{i,j} = \cos(s_{i-1})\sin(t_{j-1}), \qquad [(\mathbf{q}^{(0)})_3]_{i,j} = \sin(s_{i-1}), \tag{3.2}$$

where $1 \le i \le 4$, $1 \le j \le 7$, $s_m = -\frac{\pi}{2} + m\frac{\pi}{3}$, $m = 0,1,2,3$ and $t_n = n\frac{\pi}{3}$, $n = 0,1,2,3,4,5,6$. Since the s_m and t_n values are equally spaced with step size $\frac{\pi}{3}$, we select $\lambda = \frac{\pi}{3}$. Definition (3.2) implies that the vertices of the first and last line of $\mathbf{q}^{(0)} = \big((\mathbf{q}^{(0)})_1, (\mathbf{q}^{(0)})_2, (\mathbf{q}^{(0)})_3\big)$ are assumed to be topologically identical, namely they have the same coordinates, to define the ellipsoid's poles of coordinates $(0,0,-1)$ and $(0,0,1)$ (Figure 3). But, although the initial mesh contains only fourteen distinct points (Figure 4 (a)), the subdivision rules are blind to the topological identification. Thus, they are virtually applied to a mesh with twenty-eight vertices. (While the vertices of the mesh in Figure 4 (a) are apparently of valence 5, they actually have valence 6 due to the poles that are"multiple" vertices (Figure 3 (a)).

Remark 3.2. *The poles are preserved during the subdivision process. However, if the initial mesh is deformed, additional conditions are required in order to keep the mesh closed and smooth at the poles.*

3.1.2. Generation of Blob-Like Shapes from a Triangular Mesh Without Poles

It is possible as well to consider only six vertices, thus applying the extraordinary refinement rules of Figure 2 to an octahedron. The corresponding limit surface then takes an ellipsoidal shape. In Figure 5 (a) and (b), we show the blob-like shapes obtained from the regular octahedrons in the first row. We used $\lambda = \frac{\pi}{2}$ to define $v^{(k)}$ as in (2.4). Moreover, if the BLOB scheme is applied to an arbitrary convex octahedron, we can produce a rich collection of blob-like shapes, in particular, all affine transformations of the approximate sphere (Figure 5 (c) and (d)).

Remark 3.3. *The initial mesh can be non convex. The convexity is only required to obtain a blob-like shape.*

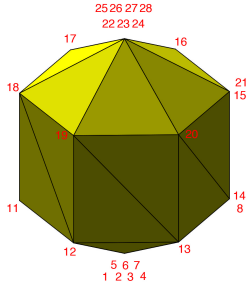

(a) Mesh with identified vertices.

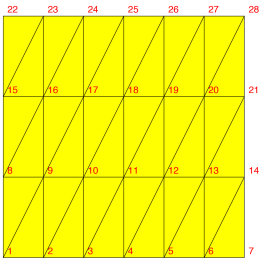

(b) Flat image of (a).

Figure 3: 3D triangular mesh defined by twenty-eight vertices.

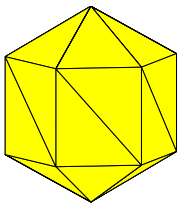

(a) Initial mesh.

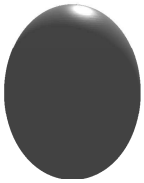

(b) Limit surface of the BLOB scheme.

Figure 4: Generation of an exact ellipsoid (b) starting from a regular triangular mesh with twenty-eight vertices, of which only fourteen are distinct (a).

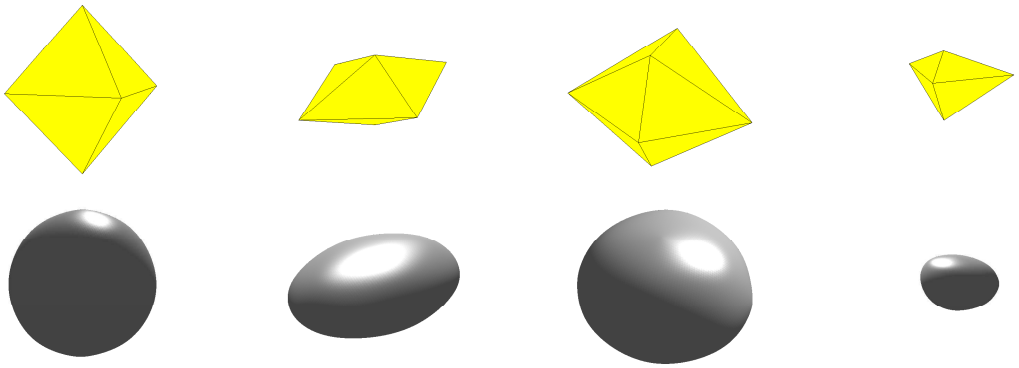

(a) Approximate sphere. (b) Approximate ellipsoid. (c) Blob-like shape. (d) Blob-like shape.

Figure 5: Initial triangular meshes (first row) and corresponding limit surfaces (second row) obtained by the BLOB scheme with extraordinary rules.

Level k	Vertices of the subdivided regular mesh with poles	Vertices of the subdivided octahedron
0	28	6
1	91	18
2	325	66
3	1225	258
4	4753	1026
5	18721	4098
6	74305	16386
7	296065	65538
8	1181953	262146

Table 1: Number of vertices of the kth-level meshes.

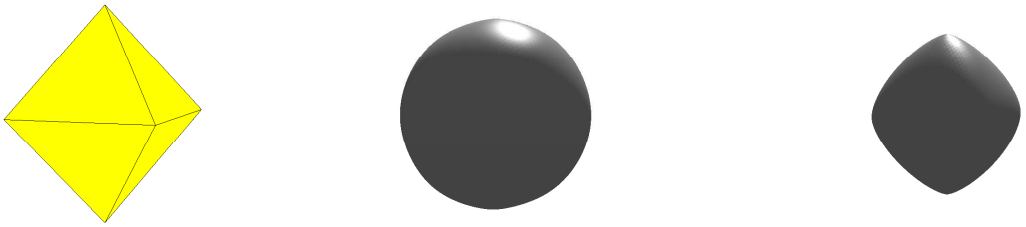

(a) Initial mesh. (b) Limit surface of the BLOB scheme. (c) Limit surface of Loop's scheme.

Figure 6: Approximation of the unit sphere obtained with (b) the BLOB scheme and (c) Loop's scheme when using the regular octahedron (a) as initial mesh.

3.1.3. Comparison

The number of vertices of the triangular meshes obtained at each subdivision step differs significantly when generating exact and approximate spheres. On one hand, the kth-level mesh obtained from the initial 28-point regular mesh with poles by applying the regular refinement rules in Figure 1 contains $18 \cdot 4^k + 9 \cdot 2^k + 1$ vertices. On the other hand, the number of vertices obtained by applying the extraordinary refinement rules in Figure 2 on an octahedron is only $4^{k+1} + 2$. In Table 1, we compare these two numbers for subdivision levels $k = 0, \ldots, 8$. We observe that the use of regular meshes to construct exact ellipsoids requires more initial vertices than those that are effectively needed if we allow the initial mesh to contain extraordinary vertices. As the vertices will be the control points of the deformable model, we certainly prefer to use the octahedron as initial mesh.

3.1.4. Comparison with Loop's Scheme

If we refine the regular octahedron using Loop's subdivision scheme [19], the shape that we obtain in the limit is more distant from the unit sphere than if we use the proposed BLOB scheme. We denote by $\mathbf{C}$ the center of gravity of the octahedron, which is the center of the circumscribed sphere. We denote by $\mathbf{f}^{(k)}$ the set of points, of cardinality $\#\mathbf{f}^{(k)}$, that define the subdivision mesh at the kth step. We say that a subdivision scheme produces a better approximation of the unit sphere if it defines a smaller error $\varepsilon = \lim_{k \to \infty} \varepsilon_k$, where

$$\varepsilon_k = \max_{i=1,\ldots,\#\mathbf{f}^{(k)}} |\mathbf{C} - \mathrm{f}_i^{(k)}| - \min_{i=1,\ldots,\#\mathbf{f}^{(k)}} |\mathbf{C} - \mathrm{f}_i^{(k)}|.$$

It turns out that the error 0.01 obtained for the BLOB scheme is almost eight times smaller than the error 0.08 produced by Loop's scheme (Figure 6).
If we insist in letting Loop's scheme match the quality of the BLOB scheme, then we need to consider a starting mesh with many more vertices than the octahedron. Precisely, we need to consider an initial mesh defined by 258 vertices (Figure 7).

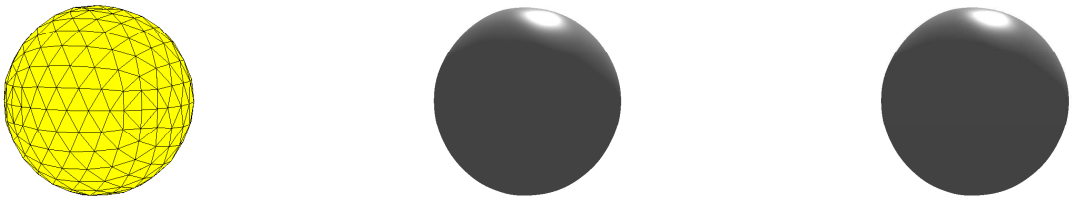

(a) Initial mesh. (b) Limit surface of the BLOB scheme. (c) Limit surface of Loop's scheme.

Figure 7: Approximation of the unit sphere obtained with (b) the BLOB scheme and (c) Loop's scheme when applied to an initial mesh consisting of 258 vertices (a).

This suggests that the BLOB scheme will be more accurate when delineating spherical shapes with a small number of initial vertices (Figure 9 (b)). As more control points are included, the two schemes will produce outcomes of equivalent quality.

3.2. Affine Invariance

The property of affine invariance means that the geometry of the limit surface produced by the subdivision scheme changes in synchrony with any affine transformation that would be applied to the initial mesh. When applied on $\mathcal{R}^{(0)}$, the affine invariance of the BLOB scheme follows from the capability of reproducing Π_1^2, as stated in Proposition 3.1 [1, 4]. Near extraordinary vertices, affine invariance is also achieved since the entries in each row of the matrix $\tilde{\mathbf{S}}_k$ defined in (2.6) sum up to 1 [1, 23].

3.3. Convergence and Smoothness

Convergence and smoothness of the BLOB scheme in the neighborhood of a regular and extraordinary vertex are investigated by means of the theoretical results proposed in [3, 5].

3.3.1. Analysis in Regular Regions of the Mesh

Proposition 3.4. *The BLOB scheme converges to C^4 limit surfaces when applied to regular triangular meshes.*

The proof of Proposition 3.4 is given in Appendix B.

3.3.2. Analysis in the Vicinity of Extraordinary Vertices

To study convergence and smoothness of the BLOB scheme in the vicinity of an extraordinary vertex of valence 4, we apply the theoretical results in [5]. More precisely, we prove Proposition 3.5 in Appendix C.

Proposition 3.5. *When applied to triangular meshes with extraordinary vertices of valence 4, the BLOB scheme converges to limit surfaces that are G^1-continuous at the limit points of the extraordinary vertices.*

4. Deformable Models for Biomedical Images

The BLOB scheme can be exploited to efficiently construct a deformable model with sphere-like topology. The surface $\boldsymbol{\sigma}$ of the deformable model is defined by $\lim_{k\to+\infty} \mathcal{M}^{(k)}$, with $\mathcal{M}^{(k)}$ in (2.1), $\{\mathcal{S}_n,\, n = 0, \ldots, k-1\}$ the subdivision operators of the BLOB scheme and $\mathcal{M}^{(0)}$ the (possibly refined) octahedron (Figure 8).

Remark 4.1. *For the implementation of the deformable model, we select a suitable resolution level $k_{\mathrm{f}} > 0$ and use the k_{f}-level mesh $\mathcal{M}^{(k_{\mathrm{f}})}$ as a discretization of the surface $\boldsymbol{\sigma}$. The mesh $\mathcal{M}^{(k_{\mathrm{f}})}$ is obtained by (2.1) after the application of k_{f} subdivision operators.*

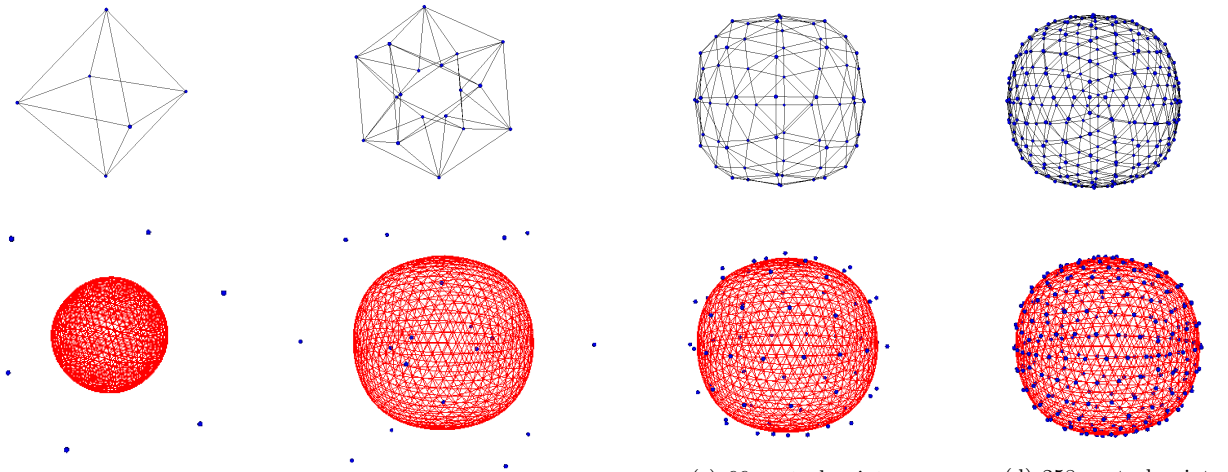

(a) 6 control points. (b) 18 control points. (c) 66 control points. (d) 258 control points.

Figure 8: First row: initial mesh $\mathcal{M}^{(0)}$. Second row: fourth-level discretization of the surface $\boldsymbol{\sigma}$ (red mesh) and its control points (blue dots).

The generated surface is then iteratively deformed until the boundary of the object is reached. We denote the vertices $\mathbf{f}^{(0)}$ of $\mathcal{M}^{(0)}$ as the control points of $\boldsymbol{\sigma}$. The shape of $\boldsymbol{\sigma}$ is entirely encoded by these points. To attract $\boldsymbol{\sigma}$ towards the surface of interest in the image, we locally adjust the control points $\mathbf{f}^{(0)}$. This is done either manually or automatically by minimizing the energy functional

$$\mathcal{E}_{\boldsymbol{\sigma}} = -\oiint_{\boldsymbol{\sigma}} \boldsymbol{\nabla} g \cdot \mathrm{d}\boldsymbol{\sigma},$$

where $\boldsymbol{\nabla} g$ is the image gradient and $\mathrm{d}\boldsymbol{\sigma}$ is the vector differential of the area. This functional consists in an image energy that is based on gradient information contained in the data [14, 28]. We use a Powell-like line-search method [24] to find the optimum $\mathbf{f}^{(0)}_{\mathrm{opt}} = \arg\min_{\mathbf{f}^{(0)}} \mathcal{E}_{\boldsymbol{\sigma}}$. The optimizer proceeds as follows: For each control point, a direction is chosen depending on the partial derivatives of the energy. Then, the control point is displaced along the selected direction to minimize the energy. The process is repeated until convergence. The use of few control points accelerates the optimization, while the ability of the model to approximate complex shapes improves as the number of control points increases. Thus, a tradeoff has to be made between accuracy and fast optimization. The image gradient $\boldsymbol{\nabla} g$ is precomputed, which accelerates the segmentation process and decreases the memory requirements.
In the following, we first show the advantage of describing the surface $\boldsymbol{\sigma}$ by means of the BLOB scheme instead of Loop's scheme. Then, we illustrate the use of this deformable model through several biomedical applications. The experiments were carried out on a 1.7 GHZ processor with 8 GB RAM. We used the fine-resolution mesh $\mathcal{M}^{(4)}$ for the discretization of $\boldsymbol{\sigma}$.

4.1. Comparison with Loop's Scheme

We saw in Section 3.1.4 that the improvement of BLOB over Loop's scheme lies in the fact that it better approximates the sphere starting from an initial mesh with few vertices. Both schemes cannot be distinguished when the initial mesh has 258 vertices. The goal of this section is to compare the accuracy of the deformable model for the delineation of structures with a spherical shape when 1) we describe the surface by either scheme; 2) we vary the number of control points. We carried out an experiment in which, for each scheme, we delineated a spherical nucleus (Figure 9 (a)) using 6 control points. We used the Jaccard index to measure the overlap between the deformed mesh and the ground truth. For two sets A and B, it is defined as $J = \frac{|A \cap B|}{|A \cup B|}$. Clearly, $0 \leq J \leq 1$, and the maximum overlap is described by $J = 1$. The results and corresponding Jaccard indices are shown in Figure 9 (b). We repeated the experiment with 258

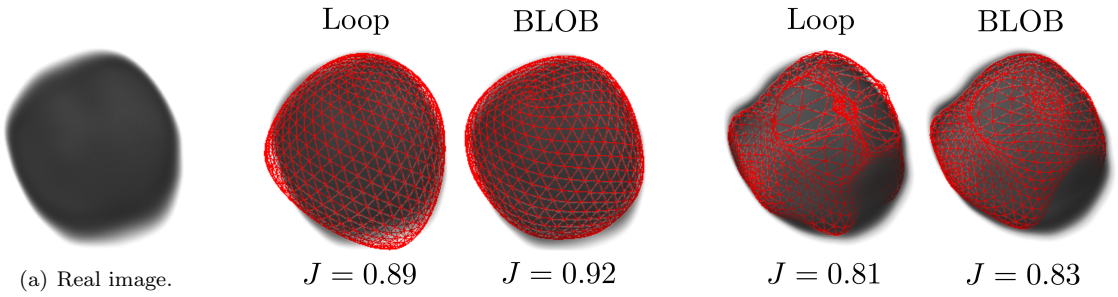

(a) Real image. (b) 6 control points. (c) 258 control points.

Figure 9: Delineations of a spherical nucleus (a) when the surface was described by either scheme. We used 6 (b) and 258 (c) control points.

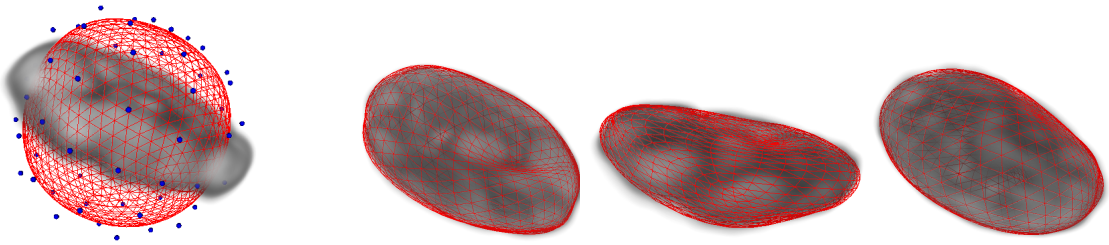

(a) Initial position of $\boldsymbol{\sigma}$. (b) Outcome of the delineation.

Figure 10: Characterization of the nucleus of a neuron in 3D microscopic images. Red mesh: fourth-level discretization of the surface $\boldsymbol{\sigma}$. Blue dots: control points.

control points. However, the resulting meshes were poor (Figure 9 (c)). As the control points were too dense compared to the size of the object, the optimization algorithm failed to reach an acceptable local optimum. This lead to a bad distribution of the vertices. Hence, for small structures with a sphere-like topology, we have a more robust and accurate deformable model when using the BLOB scheme with few control points.

4.2. Biological Images

4.2.1. Characterization of a Nucleus

After having delineated a nucleus, we get direct access to properties such as symmetry, mean intensity, and curvature. In Figure 10, we report the result of the automatical delineation of the nucleus of the neuron of a rat in 3D microscopic images [7]. The shape of the nucleus has many details (concavities); hence, as starting mesh $\mathcal{M}^{(0)}$, we used a refined octahedron with 66 control points (Figure 8 (c)). The delineation was executed in 20 seconds. The initialization of the deformable model is shown in Figure 10 (a) and the outcome is illustrated in Figure 10 (b).

4.3. Medical Images

4.3.1. Characterization of the Total Intracranial Volume

The total intracranial volume (TIV) is an important measure for volumetric analyses of the brain [20]. It is used in medicine to detect temporal morphological changes related to neurological diseases [26]. However, TIV algorithms are challenging because the brain contains many concavities such as the convoluted areas around the temporal lobe and cerebellum. In a 3D MRI scan, we performed the automatic delineation of the TIV of a human brain using the initial mesh shown in Figure 8 (d). The average time for the computation was less than 75 seconds. The initialization is given in Figure 11 (a). The result is illustrated in Figure 11 (b).

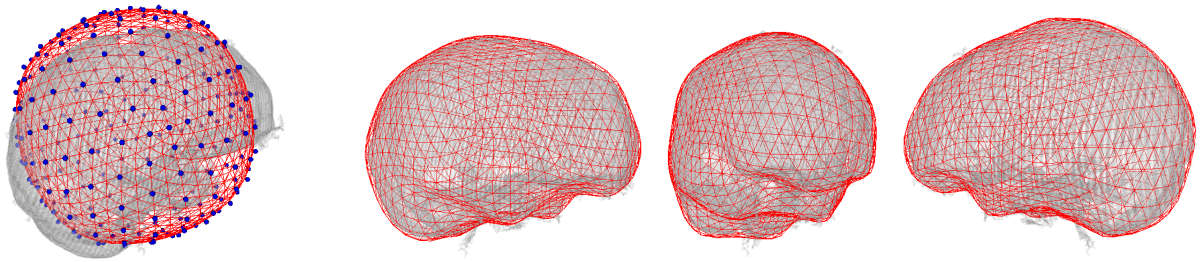

(a) Initial position of $\boldsymbol{\sigma}$. (b) Outcome of the delineation.

Figure 11: TIV delineation in a 3D MRI volume. Red mesh: fourth-level discretization of the surface $\boldsymbol{\sigma}$; Blue dots: control points.

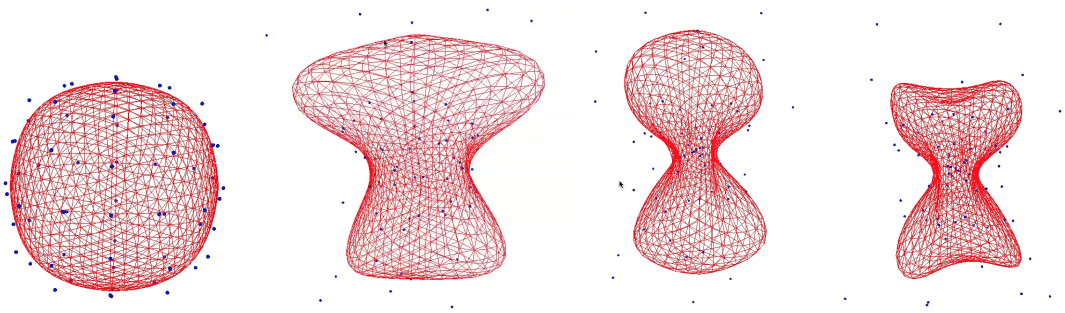

Figure 12: Deformation of the sphere by user interaction. Blue dots: control points for user interaction.

4.3.2. User-Interactive Modeling

We finally illustrate how a surface can be manually modified to design a shape of interest, starting from an approximate sphere[1]. Different steps of the modeling of a bone structure are shown in Figure 12.

5. Conclusion

We have proposed an affine-invariant non-stationary subdivision scheme, called the BLOB scheme, capable of producing G^1-continuous blob-like surfaces. The refinement process is started from a convex octahedron. The choice of this octahedron as starting mesh is motivated by two facts. First, since we are interested in blob-like structures, it is natural to consider control meshes with sphere-like topology. Second, to reduce the complexity of the deformable model, it is appropriate to use as few control points as possible. The benefits provided by the new subdivision scheme in the field of biomedical imaging are related to its efficiency to characterize 3D biomedical structures with sphere-like topology.

Acknowledgments

A. Badoual, D. Schmitter, and M. Unser are funded by the Swiss National Science Foundation under Grant 200020-162343.

[1] A video that illustrates the modeling of a bone is available at http://bigwww.epfl.ch/demo/subdivision-surfaces/

Appendix A. Proof of Proposition 3.1

Let $\Lambda_\lambda = \{(0,\, \lambda,\, -\lambda) \;:\; \lambda \in (0,\pi) \cup \mathrm{i}(0, 2\mathrm{acosh}(500))\}$, $\Theta = \Lambda_\lambda \times \Lambda_\lambda$, and $\Gamma_1 = \{(\gamma_1,\gamma_2) \in \mathbb{N}^2 : 0 \leq \gamma_1+\gamma_2 \leq 1\}$. We consider the space of exponential polynomials $EP_{(\Gamma_1,\Theta)}$ in (3.1) and the set

$$\begin{aligned}\mathcal{V}_{k,\Theta} = \;& \big\{(-1,1),(1,-1),(-1,-1),(-\mathrm{e}^{\frac{\pm\lambda}{2^{k+1}}},1),(\mathrm{e}^{\frac{\pm\lambda}{2^{k+1}}},-1),(-\mathrm{e}^{\frac{\pm\lambda}{2^{k+1}}},-1),(-1,\mathrm{e}^{\frac{\pm\lambda}{2^{k+1}}}),(1,-\mathrm{e}^{\frac{\pm\lambda}{2^{k+1}}}),\\ & (-1,-\mathrm{e}^{\frac{\pm\lambda}{2^{k+1}}}),(-\mathrm{e}^{\frac{\pm\lambda}{2^{k+1}}},\mathrm{e}^{\frac{\pm\lambda}{2^{k+1}}}),(\mathrm{e}^{\frac{\pm\lambda}{2^{k+1}}},-\mathrm{e}^{\frac{\pm\lambda}{2^{k+1}}}),(-\mathrm{e}^{\frac{\pm\lambda}{2^{k+1}}},-\mathrm{e}^{\frac{\pm\lambda}{2^{k+1}}}),(-\mathrm{e}^{\frac{\pm\lambda}{2^{k+1}}},\mathrm{e}^{\frac{\mp\lambda}{2^{k+1}}}),\\ & (\mathrm{e}^{\frac{\pm\lambda}{2^{k+1}}},-\mathrm{e}^{\frac{\mp\lambda}{2^{k+1}}}),(-\mathrm{e}^{\frac{\pm\lambda}{2^{k+1}}},-\mathrm{e}^{\frac{\mp\lambda}{2^{k+1}}})\big\}.\end{aligned}$$

In the submesh $\mathcal{R}^{(0)}$, the BLOB-subdivision scheme generates exponential polynomials from the space $EP_{(\Gamma_1,\Theta)}$, if

$$D^{(\gamma_1,\gamma_2)} a_*^{(k)}(\nu_1,\nu_2) = 0, \quad \forall (\nu_1,\nu_2) \in \mathcal{V}_{k,\Theta}, \quad (\gamma_1,\gamma_2) \in \Gamma_1, \quad \forall k \in \mathbb{N}, \tag{A.1}$$

where $D^{(\gamma_1,\gamma_2)} = \frac{\partial^{\gamma_1}}{\partial z_1^{\gamma_1}} \frac{\partial^{\gamma_2}}{\partial z_2^{\gamma_2}}$ is the directional derivative of the symbol along (γ_1,γ_2) [4, Proposition 4.2]. The kth-level symbol $a_*^{(k)}(z_1,z_2)$ given in (2.5) is such that condition (A.1) is satisfied. Hence, the BLOB scheme generates $EP_{(\Gamma_1,\Theta)}$.

In the submesh $\mathcal{R}^{(0)}$, the BLOB scheme reproduces $\Pi_1^2 = \mathrm{span}\,\{1,\, x,\, y\}$ if it is $EP_{(\Gamma_1,0)}$-generating and if its kth-level symbol satisfies [4, Theorem 4.4]

$$a_*^{(k)}(1,1) = 4, \qquad D^{(1,0)} a_*^{(k)}(1,1) = 0, \qquad D^{(0,1)} a_*^{(k)}(1,1) = 0, \quad \forall k \in \mathbb{N}. \tag{A.2}$$

As the scheme is $EP_{(\Gamma_1,\Theta)}$-generating, it is in particular $EP_{(\Gamma_1,0)}$-generating. Using (2.5), we see that (A.2) is also satisfied. Thus, the BLOB scheme reproduces Π_1^2 with respect to the parameterization $\{\mathbf{T}^{(k)}, k \in \mathbb{N}\}$, $\mathbf{T}^{(k)} = \{\mathbf{t}_{\boldsymbol{\alpha}}^{(k)} = \frac{\boldsymbol{\alpha}}{2^k}, \boldsymbol{\alpha} \in \mathbb{Z}^2\}$.

Appendix B. Proof of Proposition 3.4

We first need to recall [3, Definition 3] and [6, Definition 7].

Definition B.1. *[3, Definition 3] Let $\mathcal{Z} = \{(-1,1),(1,-1),(-1,-1)\}$ and let $D^{(\gamma_1,\gamma_2)}$ be the directional derivative along (γ_1,γ_2). A non-stationary, bivariate subdivision scheme $\mathcal{S}$ identified by the sequence of symbols $\{a_*^{(k)}(\boldsymbol{z}),\, k \in \mathbb{N}\}$, $\boldsymbol{z} \in (\mathbb{C}\backslash\{0\})^2$, is said to satisfy the approximate sum rules of order $r+1$, $r \in \mathbb{N}$, if the sequences $\{\mu_k,\, k \in \mathbb{N}\}$ and $\{\delta_k,\, k \in \mathbb{N}\}$, with*

$$\mu_k = \left|a_*^{(k)}(1,1) - 4\right| \qquad \text{and} \qquad \delta_k = \max_{0\leq\gamma_1+\gamma_2\leq r} \max_{(\zeta_1,\zeta_2)\in\mathcal{Z}} 2^{-k(\gamma_1+\gamma_2)} \left|D^{(\gamma_1,\gamma_2)} a_*^{(k)}(\zeta_1,\zeta_2)\right|$$

satisfy

$$\sum_{k=0}^{\infty} \mu_k < +\infty \qquad \text{and} \qquad \sum_{k=0}^{\infty} 2^{kr}\, \delta_k < +\infty.$$

Definition B.2. *[6, Definition 7] A stationary subdivision scheme $\bar{\mathcal{S}}$ and a non-stationary one $\mathcal{S}$ are termed asymptotically similar if the sequences $\{\mathbf{a}\}$ and $\{\mathbf{a}^{(k)},\, k \in \mathbb{N}\}$ of subdivision masks have the same support $\mathcal{J}$ (i.e., $\mathrm{a}_{\boldsymbol{\alpha}}^{(k)} = \mathrm{a}_{\boldsymbol{\alpha}} = 0$ for all $\boldsymbol{\alpha} \notin \mathcal{J}$) and satisfy $\lim_{k\to+\infty} \mathrm{a}_{\boldsymbol{\alpha}}^{(k)} = \mathrm{a}_{\boldsymbol{\alpha}}$, $\forall \boldsymbol{\alpha} \in \mathcal{J}$.*

To prove that the BLOB scheme converges to C^4 limit surfaces when applied to regular triangular meshes, we have to show that it is asymptotically similar to a stationary, convergent, bivariate subdivision scheme whose basic limit function is C^4 [3, Corollary 4] and that it satisfies the approximate sum rules of order 5. The proof of this first result is based on Proposition B.3.

Proposition B.3. *The stationary counterpart of the BLOB scheme converges to C^4 limit surfaces when applied to regular triangular meshes.*

Proof: We derive the stationary counterpart of the BLOB scheme by computing the limit of its local rules when $k \to +\infty$. Since $\lim_{k\to+\infty} v^{(k)} = 1$ for all $\lambda \in [0,\pi) \cup \mathrm{i}(0, 2\mathrm{acosh}(500))$, it follows that the stationary counterpart of the BLOB scheme applied on $\mathcal{R}^{(0)}$ is identified by the mask

$$\mathbf{a} = \lim_{k\to+\infty} \mathbf{a}^{(k)} = \begin{pmatrix} 0 & 0 & 0 & \frac{1}{128} & \frac{3}{128} & \frac{3}{128} & \frac{1}{128} \\ 0 & 0 & \frac{3}{128} & \frac{3}{32} & \frac{9}{64} & \frac{3}{32} & \frac{3}{128} \\ 0 & \frac{3}{128} & \frac{9}{64} & \frac{39}{128} & \frac{39}{128} & \frac{9}{64} & \frac{3}{128} \\ \frac{1}{128} & \frac{3}{32} & \frac{39}{128} & \frac{7}{16} & \frac{39}{128} & \frac{3}{32} & \frac{1}{128} \\ \frac{3}{128} & \frac{9}{64} & \frac{39}{128} & \frac{39}{128} & \frac{9}{64} & \frac{3}{128} & 0 \\ \frac{3}{128} & \frac{3}{32} & \frac{9}{64} & \frac{3}{32} & \frac{3}{128} & 0 & 0 \\ \frac{1}{128} & \frac{3}{128} & \frac{3}{128} & \frac{1}{128} & 0 & 0 & 0 \end{pmatrix}. \tag{B.1}$$

The associated symbol is

$$a_*(z_1, z_2) = \lim_{k\to+\infty} a_*^{(k)}(z_1, z_2) = \frac{1}{128\, z_1^3 z_2^3}\,(z_1+1)^3\,(z_2+1)^3\,(z_1 z_2+1)^3. \tag{B.2}$$

The result of Proposition B.3 follows by observing that the Laurent polynomial $a_*(z_1, z_2)$ in (B.2) is the symbol of the C^4 and Π_5^2-generating subdivision scheme proposed in [13, Example 5, case 3]. ■

In light of Proposition B.3, the BLOB scheme is asymptotically similar to the C^4 stationary subdivision scheme with symbol $a_*(z_1, z_2)$ in (B.2). It is therefore left to prove that the BLOB scheme satisfies approximate sum rules of order 5. Indeed, since $\mu_k = 0$, the sum $\sum_{k=0}^{\infty} \mu_k$ is trivially convergent. We thus only need to show that

$$\sum_{k=0}^{\infty} 2^{4k}\,\delta_k < +\infty \qquad \text{with} \qquad \delta_k = \max_{0\le\gamma_1+\gamma_2\le 4}\ \max_{(\zeta_1,\zeta_2)\in\mathcal{Z}} 2^{-k(\gamma_1+\gamma_2)}\,\left|D^{(\gamma_1,\gamma_2)}\,a_*^{(k)}(\zeta_1,\zeta_2)\right|.$$

From Proposition 3.1, we already know that the BLOB scheme generates the space $EP_{(\Gamma_1,\Theta)}$ defined by (3.1). This means that its kth-level symbol $a_*^{(k)}(z_1, z_2)$ satisfies

$$a_*^{(k)}(\zeta_1,\zeta_2) = D^{(1,0)}a_*^{(k)}(\zeta_1,\zeta_2) = D^{(0,1)}a_*^{(k)}(\zeta_1,\zeta_2) = 0 \qquad \text{for all } (\zeta_1,\zeta_2) \in \mathcal{Z}.$$

Thus, for the computation of δ_k, we can just consider $\max_{2\le\gamma_1+\gamma_2\le 4}\ \max_{(\zeta_1,\zeta_2)\in\mathcal{Z}} 2^{-k(\gamma_1+\gamma_2)}\,\left|D^{(\gamma_1,\gamma_2)}\,a_*^{(k)}(\zeta_1,\zeta_2)\right|$, which yields

$$\max_{2\le\gamma_1+\gamma_2\le 4}\ \max_{(\zeta_1,\zeta_2)\in\mathcal{Z}} 2^{-k(\gamma_1+\gamma_2)}\,\left|D^{(\gamma_1,\gamma_2)}\,a_*^{(k)}(\zeta_1,\zeta_2)\right| = \begin{cases} 2^{-4k}\,\frac{3\left|(v^{(k)}-1)(v^{(k)}-5)\right|}{(v^{(k)}+1)^2}, & v^{(k)} < \frac{7}{3} \\ 2^{-4k}\,\frac{6(v^{(k)}-1)^2}{(v^{(k)}+1)^2}, & v^{(k)} \ge \frac{7}{3}. \end{cases}$$

Focusing first on the case $v^{(k)} < \frac{7}{3}$, we find that

$$\sum_{k=0}^{\infty} 2^{4k}\delta_k = \sum_{k=0}^{\infty} \frac{3\left|(v^{(k)}-1)(v^{(k)}-5)\right|}{(v^{(k)}+1)^2}.$$

Thus, recalling the definition of $v^{(k)}$ in (2.4), and letting c be some positive constant, we exploit the fact that

$$|1 - v^{(k)}| \le c\,2^{-2k}, \tag{B.3}$$

which implies that

$$\sum_{k=0}^{\infty} 2^{4k}\delta_k = \sum_{k=0}^{\infty} \frac{3\left|(v^{(k)}-1)(v^{(k)}-5)\right|}{(v^{(k)}+1)^2} \le c \sum_{k=0}^{\infty} \left|v^{(k)} - 1\right| < +\infty.$$

With a similar reasoning, we can also show that, when $v^{(k)} \geq \frac{7}{3}$,

$$\sum_{k=0}^{\infty} 2^{4k}\delta_k = \sum_{k=0}^{\infty} \frac{6(v^{(k)}-1)^2}{(v^{(k)}+1)^2} \leq c \sum_{k=0}^{\infty} (v^{(k)}-1)^2 < +\infty.$$

Hence, the BLOB scheme satisfies approximate sum rules of order 5. We can thus conclude that the BLOB scheme is C^4-convergent (it converges to C^4 limit surfaces) when applied to regular triangular meshes.

Appendix C. Proof of Proposition 3.5

To prove that the BLOB scheme is convergent and produces G^1-continuous surfaces at the limit points of extraordinary vertices of valence 4, we need to prove that the BLOB scheme and its stationary counterpart satisfy the assumptions of Theorem C.1.

Theorem C.1. *[5, Theorems 4.6 and 4.8] Let $\mathcal{E}^{(0)}$ denote the neighborhood of an extraordinary element of valence n. Let $\mathcal{S}$ be a non-stationary subdivision scheme whose action in $\mathcal{E}^{(0)}$ is described by the matrix sequence $\{\tilde{\mathbf{S}}_k\}$ and let $\bar{\mathcal{S}}$ be a stationary subdivision scheme that in $\mathcal{E}^{(0)}$ is identified by $\{\tilde{\mathbf{S}}\}$. Moreover, let $\mathbf{S}_k$ and $\mathbf{S}$ be the block-circulant matrices possessing the same eigenvalues as $\tilde{\mathbf{S}}_k$ and $\tilde{\mathbf{S}}$ and, in case the extraordinary element is an extraordinary vertex, $(n-1)$ additional null eigenvalues. Assume that*

(i) $\bar{\mathcal{S}}$ is C^1-convergent in $\mathcal{R}^{(0)}$ with symbol $a_*(\boldsymbol{z})$ containing the factor $(1+z_1)(1+z_2)$, and G^1-convergent in $\mathcal{E}^{(0)}$;

(ii) $\mathcal{S}$ is defined in $\mathcal{R}^{(0)}$ by the symbols $\{a_*^{(k)}(\boldsymbol{z})\}$ where each $a_*^{(k)}(\boldsymbol{z})$ contains the factor $(1+z_1)(1+z_2)$;

(iii) $\mathcal{S}$ is asymptotically equivalent of order 1 to $\bar{\mathcal{S}}$ in $\mathcal{R}^{(0)}$;

(iv) in $\mathcal{E}^{(0)}$, the matrices $\mathbf{S}_k$ and $\mathbf{S}$ satisfy $\|\mathbf{S}_k - \mathbf{S}\|_\infty \leq \frac{\mathcal{C}}{\sigma^k}$, where $\mathcal{C}$ is some finite positive constant and $\sigma > \frac{1}{\lambda_1} > 1$ with $\lambda_1 \in \mathbb{R}_+$ the subdominant eigenvalue of $\mathbf{S}$ which is double and non-defective.

Then, for all bounded initial data, the non-stationary subdivision scheme $\mathcal{S}$ is convergent in $\mathcal{E}^{(0)}$ and produces a tangent-plane continuous surface at the limit points of extraordinary elements.

A gist of the proof of Theorem C.1 is given in Appendix D. We start by considering Assumption (*i*). We already know that the stationary counterpart $\bar{\mathcal{S}}$ of the BLOB scheme is C^1-convergent in $\mathcal{R}^{(0)}$ with symbol $a_*(\boldsymbol{z})$ and that it contains the factor $(1+z_1)(1+z_2)$ (see Proposition B.3 and (B.2)). To prove that $\bar{\mathcal{S}}$ is G^1-convergent in $\mathcal{E}^{(0)}$, we exploit Theorem C.2.

Theorem C.2. *[29, Theorem 3.1] Let $\bar{\mathcal{S}}$ be a stationary subdivision scheme identified by the block-circulant matrix $\{\tilde{\mathbf{S}}\}$ and let $\lambda_0, \ldots, \lambda_{N-1}$ be its eigenvalues with $|\lambda_0| \geq |\lambda_1| \geq \cdots \geq |\lambda_{N-1}|$. Let the subdominant eigenvalue λ_1 be real with geometric multiplicity 2. If $\lambda_1 = \lambda_2$, $\lambda_0 = 1 > |\lambda_1| > |\lambda_3|$, and moreover, the characteristic map of $\bar{\mathcal{S}}$ is regular and injective, then the limiting surface is C^1-continuous for almost all initial control meshes.*

To apply [29, Theorem 3.1], we need to construct the subdivision matrix $\tilde{\mathbf{S}}$, study its eigenvalues and the associated characteristic map. Using the fact that $\lim_{k\to+\infty} v^{(k)} = 1$ for all $\lambda \in [0,\pi) \cup \mathrm{i}(0, 2\mathrm{acosh}(500))$, it follows that $\tilde{\mathbf{S}}$ is given by

$$\tilde{\mathbf{S}} = \lim_{k\to+\infty} \tilde{\mathbf{S}}_k = \left[\begin{array}{c|cccc} \frac{1}{3} & \mathbf{r}^T & \mathbf{r}^T & \mathbf{r}^T & \mathbf{r}^T \\ \hline \mathbf{s} & \mathbf{M}_0 & \mathbf{M}_1 & \mathbf{M}_2 & \mathbf{M}_3 \\ \mathbf{s} & \mathbf{M}_3 & \mathbf{M}_0 & \mathbf{M}_1 & \mathbf{M}_2 \\ \mathbf{s} & \mathbf{M}_2 & \mathbf{M}_3 & \mathbf{M}_0 & \mathbf{M}_1 \\ \mathbf{s} & \mathbf{M}_1 & \mathbf{M}_2 & \mathbf{M}_3 & \mathbf{M}_0 \end{array}\right], \quad k > 1, \tag{C.1}$$

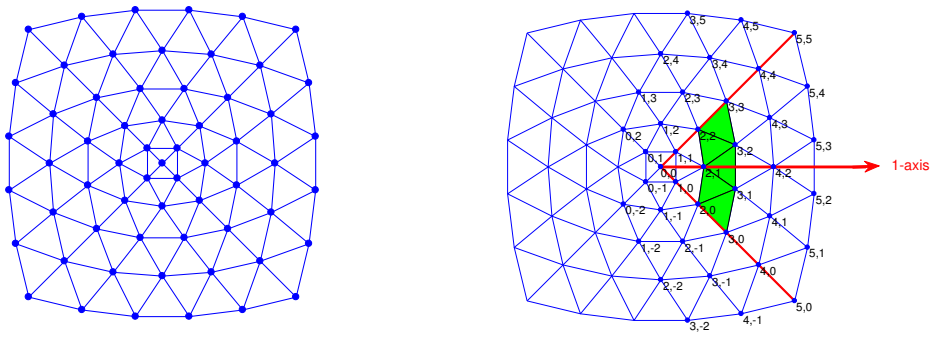

Figure C.13: Left: control net $\mathbf{c}$ of the characteristic map of the stationary counterpart of the BLOB scheme for extraordinary vertices of valence 4. Right: control points defining the first segment of the characteristic map (only the subscripts of the control points are shown). The solid green area corresponds to the first segment that constitutes the ring of regular patches defined around the extraordinary vertex. The two red lines delimiting this area identify the directions $\mathbf{e}_1$ and $\mathbf{e}_3$.

where $\mathbf{r} = \left(\frac{1}{6}, 0, 0\right)^T$, $\mathbf{s} = \left(\frac{165}{512}, \frac{3}{32}, \frac{9}{64}\right)^T$, and

$$\mathbf{M}_0 = \begin{pmatrix} \frac{39}{128} & \frac{1}{128} & \frac{3}{128} \\ \frac{7}{16} & \frac{3}{32} & \frac{3}{32} \\ \frac{39}{128} & \frac{3}{128} & \frac{9}{64} \end{pmatrix}, \; \mathbf{M}_1 = \begin{pmatrix} \frac{39}{256} & 0 & 0 \\ \frac{3}{32} & 0 & 0 \\ \frac{39}{128} & \frac{3}{128} & \frac{1}{128} \end{pmatrix}, \; \mathbf{M}_2 = \begin{pmatrix} \frac{7}{512} & 0 & 0 \\ 0 & 0 & 0 \\ \frac{3}{128} & 0 & 0 \end{pmatrix}, \; \mathbf{M}_3 = \begin{pmatrix} \frac{39}{256} & 0 & \frac{3}{128} \\ \frac{3}{32} & 0 & \frac{3}{32} \\ \frac{3}{128} & 0 & \frac{1}{128} \end{pmatrix}.$$

Before transforming $\tilde{\mathbf{S}}$ into the block-circulant matrix

$$\mathbf{S} = \mathbf{circ}(\mathbf{B}_0, \mathbf{B}_1, \mathbf{B}_2, \mathbf{B}_3) \quad \text{with} \quad \mathbf{B}_j = \begin{pmatrix} \frac{1}{12} & \mathbf{r}^T \\ \frac{\mathbf{s}}{4} & \mathbf{M}_j \end{pmatrix}, \quad j = 0, \ldots, 3$$

that has the same eigenvalues as $\tilde{\mathbf{S}}$ plus three null eigenvalues, we first extend the blocks $\mathbf{M}_j$, as well as the vectors $\mathbf{r}$ and $\mathbf{s}$, from size 3 to 15. This is actually needed to properly define the characteristic map of $\bar{\mathcal{S}}$. In fact, due to the support of the basic limit function of $\bar{\mathcal{S}}$ which, in $\mathcal{R}^{(0)}$, coincides with the C^4 bivariate three-directional box-spline defined by the set $\{\mathbf{e}_1, \mathbf{e}_1, \mathbf{e}_1, \mathbf{e}_2, \mathbf{e}_2, \mathbf{e}_2, \mathbf{e}_3, \mathbf{e}_3, \mathbf{e}_3\}$ with $\mathbf{e}_1 = (1, 0)^T$, $\mathbf{e}_2 = (0, 1)^T$, $\mathbf{e}_3 = (1, 1)^T$, the submesh $\mathcal{E}^{(0)}$ must be extended to a 5-ring neighborhood of the extraordinary vertex in order to define a full ring of regular patches around it (Figure C.13).
There follows that $\mathbf{S}$ has size (64×64), $\lambda_0 = 1$ is its unique dominant eigenvalue with corresponding eigenvector $\mathbf{1}$, $\lambda_1 = 0.3776$ is the subdominant eigenvalue with algebraic and geometric multiplicity 2, and $\lambda_3 = 0.2201$. Hence, the conditions $\lambda_1 = \lambda_2$ and $\lambda_0 = 1 > |\lambda_1| > |\lambda_3|$ of [29, Theorem 3.1] are verified.
To define the characteristic map of $\bar{\mathcal{S}}$, we extract from $\mathbf{S}$ the two eigenvectors that correspond to the subdominant eigenvalue. They are real and linearly independent. Their entries define the 2D coordinates of the control net $\mathbf{c}$ of the characteristic map, which is depicted in Figure C.13 (left). Then, once $\mathbf{c}$ is computed, the characteristic map is simply defined as the limit surface obtained by $\mathbf{c}$ using the subdivision scheme $\bar{\mathcal{S}}$.
For such a symmetric subdivision scheme, the characteristic map is made up of 4 rotationally symmetric segments. A segment is defined by a subset $\mathcal{X}$ of the 2D control points of $\mathbf{c}$. For $\bar{\mathcal{S}}$, the set $\mathcal{X}$ that defines the first segment of the characteristic map, normalized such that it is symmetric with respect to the 1-axis (Figure C.13 (right)), is given by

$$\mathcal{X} = \begin{array}{ccccccc} & & & \mathrm{c}_{3,5} & & & \\ & & \mathrm{c}_{2,4} & & \mathrm{c}_{4,5} & & \\ & \mathrm{c}_{1,3} & & \mathrm{c}_{3,4} & & \mathrm{c}_{5,5} & \\ \mathrm{c}_{0,2} & & \mathrm{c}_{2,3} & & \mathrm{c}_{4,4} & & \\ & \mathrm{c}_{1,2} & & \mathrm{c}_{3,3} & & \mathrm{c}_{5,4} & \\ \mathrm{c}_{0,1} & & \mathrm{c}_{2,2} & & \mathrm{c}_{4,3} & & \\ & \mathrm{c}_{1,1} & & \mathrm{c}_{3,2} & & \mathrm{c}_{5,3} & \\ \mathrm{c}_{0,0} & & \mathrm{c}_{2,1} & & \mathrm{c}_{4,2} & & \\ & \mathrm{c}_{1,0} & & \mathrm{c}_{3,1} & & \mathrm{c}_{5,2} & \\ \mathrm{c}_{0,-1} & & \mathrm{c}_{2,0} & & \mathrm{c}_{4,1} & & \\ & \mathrm{c}_{1,-1} & & \mathrm{c}_{3,0} & & \mathrm{c}_{5,1} & \\ \mathrm{c}_{0,-2} & & \mathrm{c}_{2,-1} & & \mathrm{c}_{4,0} & & \\ & \mathrm{c}_{1,-2} & & \mathrm{c}_{3,-1} & & \mathrm{c}_{5,0} & \\ & & \mathrm{c}_{2,-2} & & \mathrm{c}_{4,-1} & & \\ & & & \mathrm{c}_{3,-2} & & & \end{array}. \tag{C.2}$$

Now, we denote by

$$\nabla_n \, q_{\boldsymbol{\alpha}}^{(k)} = q_{\boldsymbol{\alpha}+\mathbf{e}_n}^{(k)} - q_{\boldsymbol{\alpha}}^{(k)}, \quad n = 1, 2, 3 \tag{C.3}$$

the directional difference ∇_n of the points $q_{\boldsymbol{\alpha}}^{(k)}$, $\boldsymbol{\alpha} \in \mathbb{Z}^2$. To prove that the characteristic map of $\bar{\mathbb{S}}$ is regular and injective, we state Theorem C.3.

Theorem C.3. *[30, Theorem 1] Let $\mathcal{X}$ be the control net that defines the first segment of the characteristic map and let $\mathcal{C}_n$ denote the cone of length $|\mathcal{C}_n|$ defined by*

$$\mathcal{C}_n = [\inf_{\mathrm{c_i} \in \mathcal{X}} \angle(\nabla_n \mathrm{c_i}, 1-axis), \sup_{\mathrm{c_i} \in \mathcal{X}} \angle(\nabla_n \mathrm{c_i}, 1-axis)], \quad n = 1, 2, 3.$$

For a symmetric subdivision scheme, the characteristic map is regular and injective if

- *the divided ∇_1- and ∇_3-difference schemes are scalar and use only convex combinations;*
- *none of the ∇_1- and ∇_3-differences of $\mathcal{X}$ vanish; and*
- *the cones $\mathcal{C}_1$ and $\mathcal{C}_3$ satisfy the conditions*

$$|\mathcal{C}_1 \cup \mathcal{C}_3| < \pi \qquad \text{and} \qquad \mathcal{C}_1 \cap \mathcal{C}_3 = \emptyset.$$

Since, in $\mathcal{R}^{(0)}$, the stationary counterpart of the BLOB scheme has the subdivision symbol in (B.2) and converges to C^4 limit surfaces, we can easily observe that, for all $n = 1, 2, 3$, there exists a scalar subdivision scheme using only convex combinations that maps the divided ∇_n-differences of level k, defined by (C.3), into the divided ∇_n-differences of level $k+1$. Moreover, since the points of $\mathcal{X}$ in (C.2) are pairwise distinct, it is immediate to see that none of the ∇_1- and ∇_3-differences of $\mathcal{X}$ vanishes. Finally, it is not difficult to see that the first coordinates of the points of $\mathcal{X}$ in (C.2) increase in the direction $\mathbf{e}_1$ while the second coordinates decrease in the direction $\mathbf{e}_1$ and increase in direction $\mathbf{e}_2$. Thus, the first coordinates of the ∇_1-differences and the second coordinates of the ∇_2-differences are positive, while the second coordinates of the ∇_1-differences are negative. This yields for the cones $\mathcal{C}_1$, $\mathcal{C}_2$, and $\mathcal{C}_3$, that $\mathcal{C}_1 \subseteq (-\pi/2, 0)$, $\mathcal{C}_2 \subseteq (0, \pi)$, and $\mathcal{C}_3 \subseteq (0, \pi/2)$. It follows that

$$|\mathcal{C}_1 \cup \mathcal{C}_3| < \pi \qquad \text{and} \qquad \mathcal{C}_1 \cap \mathcal{C}_3 = \emptyset.$$

Hence, we conclude that the characteristic map of the stationary BLOB scheme is regular and injective. Then, in light of [29, Theorem 3.1], the stationary counterpart of the BLOB scheme is C^1-convergent in the neighborhood of extraordinary vertices of valence 4 and, therefore, G^1-convergent, too.

To apply [5, Theorem 4.8], we need to prove that all remaining assumptions are satisfied. Assumption (*ii*) is trivially satisfied because of (2.5). Assumptions (*iii*) and (*iv*) compare the behavior of the BLOB scheme with that of its stationary counterpart. The comparison focuses on the neighborhood of regular and extraordinary vertices, separately. In the neighborhood of regular vertices, the comparison consists in showing that the subdivision masks $\mathbf{a}^{(k)}$ and $\mathbf{a}$ in (2.3) and (B.1), respectively, are asymptotically equivalent of order 1 so that they satisfy the property in Definition C.4.

Definition C.4. *[5, Definition 3.2.] The stationary subdivision scheme $\bar{\mathcal{S}}$ and the non-stationary scheme $\mathcal{S}$ are termed asymptotically equivalent of order 1 if the sequences $\{\mathbf{a}\}$ and $\{\mathbf{a}^{(k)},\ k\in\mathbb{N}\}$ of subdivision masks satisfy*

$$\sum_{k=0}^{+\infty} 2^k \max\left\{\sum_{\boldsymbol{\beta}\in\mathbb{Z}^2} |\mathrm{a}^{(k)}_{\boldsymbol{\alpha}-2\boldsymbol{\beta}} - \mathrm{a}_{\boldsymbol{\alpha}-2\boldsymbol{\beta}}| \ :\ \boldsymbol{\alpha}\in\{(0,0),(0,1),(1,0),(1,1)\}\right\} < +\infty.$$

Exploiting the identities

$$\cos(2^{-k}\lambda) = 1 - \frac{\lambda^2}{2}2^{-2k} + \frac{\lambda^4}{24}2^{-4k}\cos(\xi), \quad \xi\in(0,2^{-k}\lambda),$$

$$\cos^2(2^{-k}\lambda) = 1 - \lambda^2 2^{-2k} + \frac{\lambda^4}{3}2^{-4k}\cos(2\tilde{\xi}), \quad \tilde{\xi}\in(0,2^{-k}\lambda),$$

and

$$\cosh(2^{-k}\lambda) = 1 + \lambda^2 2^{-2k} + \frac{\lambda^4}{24}2^{-4k}\cosh(\eta), \quad \eta\in(0,2^{-k}\lambda),$$

$$\cosh^2(2^{-k}\lambda) = 1 + 2\lambda^2 2^{-2k} + \frac{\lambda^4}{3}2^{-4k}\cosh(2\tilde{\eta}), \quad \tilde{\eta}\in(0,2^{-k}\lambda),$$

given by the Lagrange form of the remainder of the Taylor expansion, we get the bounds

$$\begin{array}{lll} |a^{(k)} - \frac{7}{16}| \le \frac{\mathcal{A}}{4^k}, & |b^{(k)} - \frac{3}{32}| \le \frac{\mathcal{B}}{4^k}, & |c^{(k)} - \frac{3}{128}| \le \frac{\mathcal{C}}{4^k}, \\ |d^{(k)} - \frac{9}{64}| \le \frac{\mathcal{D}}{4^k}, & |e^{(k)} - \frac{1}{128}| \le \frac{\mathcal{E}}{4^k}, & |f^{(k)} - \frac{39}{128}| \le \frac{\mathcal{F}}{4^k}, \end{array} \tag{C.4}$$

with $\mathcal{A},\mathcal{B},\mathcal{C},\mathcal{D},\mathcal{E},\mathcal{F}$ finite positive constants independent of k. Thus, we can write that

$$\begin{array}{ll} \max\left\{\sum_{\boldsymbol{\beta}\in\mathbb{Z}^2} |\mathrm{a}^{(k)}_{\boldsymbol{\alpha}-2\boldsymbol{\beta}} - \mathrm{a}_{\boldsymbol{\alpha}-2\boldsymbol{\beta}}| \ :\ \boldsymbol{\alpha}\in\{(0,0),(0,1),(1,0),(1,1)\}\right\} & = \\ \max\left\{|a^{(k)} - \frac{7}{16}| + 6|b^{(k)} - \frac{3}{32}|,\ 4|c^{(k)} - \frac{3}{128}| + 2|d^{(k)} - \frac{9}{64}| + 2|e^{(k)} - \frac{1}{128}| + 2|f^{(k)} - \frac{39}{128}|\right\} & \le \\ \frac{1}{4^k}\max\left\{\mathcal{A} + 6\mathcal{B},\ 4\mathcal{C} + 2\mathcal{D} + 2\mathcal{E} + 2\mathcal{F}\right\}, & \end{array}$$

so that

$$\begin{array}{l} \sum_{k=0}^{+\infty} 2^k \max\left\{\sum_{\boldsymbol{\beta}\in\mathbb{Z}^2} |\mathrm{a}^{(k)}_{\boldsymbol{\alpha}-2\boldsymbol{\beta}} - \mathrm{a}_{\boldsymbol{\alpha}-2\boldsymbol{\beta}}| \ :\ \boldsymbol{\alpha}\in\{(0,0),(0,1),(1,0),(1,1)\}\right\} \ \le \\ \max\left(\mathcal{A} + 6\mathcal{B},\ 4\mathcal{C} + 2\mathcal{D} + 2\mathcal{E} + 2\mathcal{F}\right)\sum_{k=0}^{+\infty}\frac{1}{2^k} < +\infty. \end{array}$$

As a consequence, Assumption (*iii*) is satisfied.
We now focus on the neighborhood of extraordinary vertices. After transforming $\tilde{\mathbf{S}}_k$ into the block circulant matrix

$$\mathbf{S}_k = \mathbf{circ}(\mathbf{B}_0^{(k)},\mathbf{B}_1^{(k)},\mathbf{B}_2^{(k)},\mathbf{B}_3^{(k)}) \quad \text{with} \quad \mathbf{B}_j^{(k)} = \begin{pmatrix} \frac{\tilde{a}^{(k)}}{4} & (\mathbf{r}^{(k)})^T \\ \frac{\mathbf{s}^{(k)}}{4} & \mathbf{M}_j^{(k)} \end{pmatrix}, \ \ j = 0,\dots,3,$$

we write that

$$\|\mathbf{S}_k - \mathbf{S}\|_\infty \le \|\mathbf{B}_0^{(k)} - \mathbf{B}_0\|_\infty + \|\mathbf{B}_1^{(k)} - \mathbf{B}_1\|_\infty + \|\mathbf{B}_2^{(k)} - \mathbf{B}_2\|_\infty + \|\mathbf{B}_3^{(k)} - \mathbf{B}_3\|_\infty.$$

Each norm on the right-hand side can be explicitly computed and shown to satisfy the upper bounds $\|\mathbf{B}_j^{(k)} - \mathbf{B}_j\|_\infty \le \frac{\mathcal{M}_j}{4^k}$, $j = 0,...,3$ with $\mathcal{M}_j$ finite positive constants independent of k, in view of the inequalities (C.4). Hence $\|\mathbf{S}_k - \mathbf{S}\|_\infty \le \frac{\mathcal{M}}{4^k}$, with $\mathcal{M} = \mathcal{M}_0 + \mathcal{M}_1 + \mathcal{M}_2 + \mathcal{M}_3$ a finite positive constant independent of k. Observing that $\lambda_1 = 0.3776$ has algebraic and geometric multiplicity 2 and satisfies $4 > \frac{1}{\lambda_1} > 1$, we can conclude that Assumption (*iv*) is satisfied for $\sigma = 4$.
It follows that all the assumptions of Theorem C.1 are verified. Thus, the non-stationary BLOB scheme is convergent at extraordinary vertices and the limit surfaces obtained by such a scheme are G^1-continuous at the limit points of extraordinary vertices.

Appendix D. Gist of the Proof of Theorem C.1

Let us start by defining some notation and vocabulary. Since we deal with triangular meshes, we denote by Ω_k, $k \in \mathbb{N}$ the subdomain of $\mathbb{R}^2$ defined by

$$\Omega_k = \{(u,v) \in \mathbb{R}^2 \,|\, u,v \geq 0 \text{ and } 2^{-k} \leq u+v \leq 2^{1-k}\}.$$

Moreover, since we focus our analysis around an isolated extraordinary vertex of valence n, we consider the local domain consisting of n copies of Ω_k, briefly denoted by $\Omega_k \times \mathbb{Z}_n$ with $\mathbb{Z}_n = \mathbb{Z}/n\mathbb{Z}$. During the refinement process, the subdivision scheme $\mathcal{S}$ generates a sequence of regular rings $\{\mathbf{r}_k, k \in \mathbb{N}\}$, where the k-th regular ring $\mathbf{r}_k : \Omega_k \times \mathbb{Z}_n \to \mathbb{R}^3$ can be expressed in terms of a control point vector $\mathbf{d}_k$ and the associated basic limit function vector $\mathbf{\Phi}_k$.

The gist of the proof is based on the following mathematical pipeline:

- To prove convergence of $\mathcal{S}$, we have to show that, for all bounded initial vectors $\mathbf{d}_0$ (containing the vertices of $\mathcal{E}^{(0)}$), there exists a limit point $\mathbf{r}_c \in \mathbb{R}^3$ such that $\lim_{k\to+\infty} \sup_{(u,v)\in\Omega_k\times\mathbb{Z}_n} \|\mathbf{r}_k(u,v) - \mathbf{r}_c\|_\infty = 0$.
- Then, if $\mathcal{S}$ converges, $\mathbf{r} = \bigcup_{k\in\mathbb{N}} \mathbf{r}_k \cup \{\mathbf{r}_c\}$ is a surface without gap; *i.e.*, $\mathbf{r}$ is a surface that is continuous at all points including $\mathbf{r}_c$ (which is in fact $\mathbf{r}(0,0)$).
- Finally, to prove that the limit surface $\mathbf{r}$ is G^1-continuous at $\mathbf{r}_c$, we have to show that the sequence of normal vectors $\{\mathbf{n}_k(u,v) = \frac{\partial_u \mathbf{r}_k(u,v) \wedge \partial_v \mathbf{r}_k(u,v)}{\|\partial_u \mathbf{r}_k(u,v) \wedge \partial_v \mathbf{r}_k(u,v)\|_2}, (u,v) \in \Omega_k \times \mathbb{Z}_n, k \in \mathbb{N}\}$ converges uniformly to the normal vector $\mathbf{n}(\mathbf{r}_c)$ defined at the limit point $\mathbf{r}_c$, *i.e.*, $\lim_{k\to+\infty} \sup_{(u,v)\in\Omega_k\times\mathbb{Z}_n} \|\mathbf{n}_k(u,v) - \mathbf{n}(\mathbf{r}_c)\|_\infty = 0$.

To obtain the existence of the limit point $\mathbf{r}_c$, we first study the behaviour of $\{\mathbf{\Phi}_k(u,v), k \in \mathbb{N}\}$ and $\{\mathbf{d}_k, k \in \mathbb{N}\}$ when $k \to +\infty$.

We start by considering Assumptions (ii), (iii) and the fact that $\bar{\mathcal{S}}$ is C^1-convergent in $\mathcal{R}^{(0)}$ with a symbol that contains the factor $(1+z_1)(1+z_2)$ (*i.e.*, first part of Assumption (i)). These assumptions allow us to claim that $\mathcal{S}$ is C^1-convergent in $\mathcal{R}^{(0)}$, that the sequence of basic limit function vectors $\{\mathbf{\Phi}_k, k \in \mathbb{N}\}$ converges uniformly to the basic limit function vector $\bar{\mathbf{\Phi}}$ of $\bar{\mathcal{S}}$ when $k \to +\infty$, and that the sequence $\{\partial_u \mathbf{\Phi}_k, k \in \mathbb{N}\}$ (resp. $\{\partial_v \mathbf{\Phi}_k, k \in \mathbb{N}\}$) converges uniformly to $\partial_u \bar{\mathbf{\Phi}}$ (resp. $\partial_v \bar{\mathbf{\Phi}}$) when $k \to +\infty$. We call this Result (A).

The control point vector $\mathbf{d}_k$ is linked to the initial control point vector $\mathbf{d}_0$ by the relation

$$\mathbf{d}_k = \mathbf{S}^{(k)}\mathbf{d}_0 \quad \text{with} \quad \mathbf{S}^{(k)} = \mathbf{S}_{k-1}\,\mathbf{S}_{k-2} \cdots \mathbf{S}_1\mathbf{S}_0, \quad k \in \mathbb{N}^*,$$

where $\mathbf{S}_j$, $j = 0, \ldots, k-1$, is the j-th block-circulant matrix defining $\mathcal{S}$ in $\mathcal{E}^{(0)}$. Hence, to study the behaviour of $\mathbf{d}_k$ as $k \to +\infty$, we write the product matrix $\mathbf{S}^{(k)}$ in terms of the stationary matrix $\mathbf{S}$. It follows that

$$\mathbf{d}_k = \mathbf{S}^k\mathbf{d}_0 + \mathbf{y}_k, \tag{D.1}$$

where $\mathbf{y}_k$ is the corresponding residual term. Assuming convergence of $\bar{\mathcal{S}}$ in $\mathcal{E}^{(0)}$ (which is implied by the second part of Assumption (i)), for k sufficiently large, we get

$$\mathbf{S}^k\mathbf{d}_0 = \mathbf{x}_0\mathbf{q}_0^T + O(\lambda_1^k) \tag{D.2}$$

with $\mathbf{q}_0^T = \tilde{\mathbf{x}}_0^T\mathbf{d}_0$. The symbols $\tilde{\mathbf{x}}_0^T$ and $\mathbf{x}_0$ denote respectively the left and right eigenvector of $\mathbf{S}$ associated with its unique dominant eigenvalue $\lambda_0 = 1$, while $\lambda_1 \in \mathbb{R}_+$ is the subdominant eigenvalue of $\mathbf{S}$ which is assumed to be double and non-defective. Moreover under Assumption (iv), we are able to show that, when k is large enough, we have

$$\mathbf{y}_k = \mathbf{x}_0\boldsymbol{\beta}_0^T + O\left(\frac{1}{\sigma^k}\right), \tag{D.3}$$

for $\boldsymbol{\beta}_0 = (\lim_{k\to+\infty} \mathbf{y}_k)^T \frac{\mathbf{x}_0}{\|\mathbf{x}_0\|_2^2}$. Using (D.1), (D.2) and (D.3), we have that

$$\lim_{k\to+\infty} \mathbf{d}_k = \mathbf{x}_0(\mathbf{q}_0 + \boldsymbol{\beta}_0)^T. \tag{D.4}$$

Combining the result in (D.4) with Result (A), we then are able to prove the existence of the limit point $\mathbf{r}_c$, which is exactly $\mathbf{r}_c = \mathbf{q}_0 + \boldsymbol{\beta}_0$. Hence, $\mathcal{S}$ is convergent in $\mathcal{E}^{(0)}$.

We now want to prove that the limit surface $\mathbf{r}$ is G^1-continuous at $\mathbf{r}_c$. In light of the G^1-convergence of $\bar{\mathcal{S}}$ in $\mathcal{E}^{(0)}$ (*i.e.*, considering exactly the second part of Assumption (i)), we know that, for k sufficiently large,

$$S^k \mathbf{d}_0 = \mathbf{x}_0 \mathbf{q}_0^T + \lambda_1^k (\mathbf{x}_1^0 (\mathbf{q}_1^0)^T + \mathbf{x}_1^1 (\mathbf{q}_1^1)^T) + o(\lambda_1^k),$$

where $\mathbf{q}_1^0$ and $\mathbf{q}_1^1$ are vectors in $\mathbb{R}^3$, while $\mathbf{x}_1^0$ and $\mathbf{x}_1^1$ are the two linearly independent eigenvectors associated to λ_1. Thus, using the resulting asymptotic expansion

$$\mathbf{d}_k = \mathbf{x}_0 (\mathbf{q}_0^T + \boldsymbol{\beta}_0^T) + \lambda_1^k (\mathbf{x}_1^0 (\mathbf{q}_1^0)^T + \mathbf{x}_1^1 (\mathbf{q}_1^1)^T) + \boldsymbol{\theta}_k, \tag{D.5}$$

where $\boldsymbol{\theta}_k$ is a vector with all its entries behaving as $o(\lambda_1^k) + O\left(\frac{1}{\sigma^k}\right)$, we are able to show that, for k sufficiently large,

$$\mathbf{n}_k(u,v) = \operatorname{sign}\left(\det \begin{pmatrix} \partial_u \boldsymbol{\Phi}_k(u,v)^T \mathbf{x}_1^0 & \partial_u \boldsymbol{\Phi}_k(u,v)^T \mathbf{x}_1^1 \\ \partial_v \boldsymbol{\Phi}_k(u,v)^T \mathbf{x}_1^0 & \partial_v \boldsymbol{\Phi}_k(u,v)^T \mathbf{x}_1^1 \end{pmatrix} \right) \frac{((\mathbf{q}_1^0)^T \wedge (\mathbf{q}_1^1)^T) + o(1)}{\|((\mathbf{q}_1^0)^T \wedge (\mathbf{q}_1^1)^T) + o(1)\|_2}.$$

Hence, in light of Result (A) and of the fact that

$$\mathbf{n}(\mathbf{r}_c) = \operatorname{sign}\left(\det \begin{pmatrix} \partial_u \bar{\boldsymbol{\Phi}}(0,0)^T \mathbf{x}_1^0 & \partial_u \bar{\boldsymbol{\Phi}}(0,0)^T \mathbf{x}_1^1 \\ \partial_v \bar{\boldsymbol{\Phi}}(0,0)^T \mathbf{x}_1^0 & \partial_v \bar{\boldsymbol{\Phi}}(0,0)^T \mathbf{x}_1^1 \end{pmatrix} \right) \frac{(\mathbf{q}_1^0)^T \wedge (\mathbf{q}_1^1)^T}{\|(\mathbf{q}_1^0)^T \wedge (\mathbf{q}_1^1)^T\|_2},$$

we obtain that $\lim\limits_{k \to +\infty} \sup_{(u,v) \in \Omega_k \times \mathbb{Z}_n} \|\mathbf{n}_k(u,v) - \mathbf{n}(\mathbf{r}_c)\|_\infty = 0$. This proves that the limit surface $\mathbf{r}$ is G^1-continuous at $\mathbf{r}_c = \mathbf{r}(0,0)$, which ends the proof.

References

[1] L.-E. Andersson, N.F. Stewart, Introduction to the Mathematics of Subdivision Surfaces, SIAM 2010.

[2] V. Caselles, R. Kimmel, G. Sapiro, Geodesic active contours, International Journal of Computer Vision 22(1) (1997), 61–79.

[3] M. Charina, C. Conti, N. Guglielmi, V. Protasov, Regularity of non-stationary subdivision: A matrix approach, Numerische Mathematik 135(3) (2017), 639–678.

[4] M. Charina, C. Conti, L. Romani, Reproduction of exponential polynomials by multivariate non-stationary subdivision schemes with a general dilation matrix, Numerische Mathematik 127(2) (2014), 223–254.

[5] C. Conti, M. Donatelli, P. Novara, L. Romani, A linear algebra approach to the analysis of non-stationary subdivision for 2-manifold meshes with arbitrary topology, arXiv:1707.01954 [math.NA], 2017.

[6] C. Conti, N. Dyn, C. Manni, M. L. Mazure, Convergence of univariate non-stationary subdivision schemes via asymptotical similarity, Computer Aided Geometric Design 37 (2015), 1-8.

[7] S. Da Silveira, B. Schneider, C. Cifuentes-Diaz, D. Sage, T. Abbas-Terki, T. Iwatsubo, M. Unser, P. Aebischer, Phosphorylation does not prompt, nor prevent, the formation of α-synuclein toxic species in a rat model of Parkinson's disease, Human Molecular Genetics 18(5) (2009), 872–887.

[8] B. De Leener, S. Kadoury, J. Cohen-Adad, Robust, accurate and fast automatic segmentation of the spinal cord, NeuroImage 98 (2014), 528–536.

[9] R. Delgado-Gonzalo, N. Chenouard, M. Unser, Spline-based deforming ellipsoids for interactive 3D bioimage segmentation, IEEE Transactions on Image Processing 22(10) (2013) 3926-3940.

[10] T. DeRose, M. Kass, T. Truong, Subdivision surfaces in character animation, In Proceedings of the 25th Annual Conference on Computer Graphics and Interactive Techniques, 85–94, ACM New York (1998).

[11] A. Dufour, R. Thibeaux, E. Labruyere, N. Guillen, J.-C. Olivo-Marin, 3-D active meshes: Fast discrete deformable models for cell tracking in 3-D time-lapse microscopy, IEEE Transactions on Image Processing 20(7) (2011), 1925–1937.

[12] C. Gotsman, S. Gumhold, L. Kobbelt, Simplification and compression of 3D meshes, Tutorials on Multiresolution in Geometric Modelling, Part of the series Mathematics and Visualization, A. Iske, E. Quak and M.S. Floater eds. (2002), 319–361.

[13] B. Han, Classification and construction of bivariate subdivision schemes, Proceedings on Curves and Surfaces Fitting: Saint-Malo 2002, A. Cohen, J.-L. Merrien and L. L. Schumaker eds. (2003), 187–197.

[14] M. Jacob, T. Blu, M. Unser, Efficient energies and algorithms for parametric snakes, IEEE Transactions on Image Processing 13(9) (2004), 1231–1244.

[15] K. Karciauskas, J. Peters, Bicubic polar subdivision, ACM Transactions on Graphics 26(4) (2007), Article no 14.

[16] M. Kass, A. Witkin, D. Terzopoulos, Snakes: Active contour models, International Journal of Computer Vision 1(4) (1987), 321–331.

[17] M. Kaus, V. Pekar, C. Lorenz, R. Truyen, S. Lobregt, J. Weese, Automated 3D PDM construction from segmented images using deformable models, IEEE Transactions on Medical Imaging 22(8) (2003), 1005–1013.
[18] A. Lee, H. Moreton, H. Hoppe, Displaced subdivision surfaces, Proceedings of the 27th Annual Conference on Computer Graphics and Interactive Techniques, ACM Press/Addison-Wesley Publishing Co. (2000), New Yor, NY, USA, 85–94.
[19] C. Loop, Smooth subdivision surfaces based on triangles, M.S. Thesis, Department of Mathematics, University of Utah (1987).
[20] I. B. Malone, K. K. Leung, S. Clegg, J. Barnes, J.L. Whitwell, J. Ashburner, N.C. Fox, G.R. Ridgway, Accurate automatic estimation of total intracranial volume: A nuisance variable with less nuisance. Neuroimage, 2015, vol. 104, p. 366-372.
[21] K. Müller, L. Reusche, D. Fellner, Extended subdivision surfaces: Building a bridge between NURBS and Catmull-Clark surfaces, ACM Transactions on Graphics 25(2) (2006), 268–292.
[22] A. Myles, K. Karciauskas, J. Peters, Extending Catmull-Clark subdivision and PCCM with polar structures, IEEE Proceedings of the 15th Pacific Conference on Computer Graphics and Applications, (2007), Washington, DC, USA, 313–320.
[23] J. Peters, U. Reif, Subdivision Surfaces, Springer, 2008.
[24] W. Press, S. Teukolsky, W. Vetterling, and B. Flannery, Numerical Recipes: The Art of Scientific Computing. Cambridge University Press, third ed., 1986.
[25] D. Schmitter, R. Delgado-Gonzalo, G. Krueger, M. Unser, Atlas-free brain segmentation in 3D proton-density-like MRI images, International Symposium on Biomedical Imaging (2014), Beijing, People's Republic of China, April 29-May 2, 629–632.
[26] D. Schmitter, C. Gaudet-Blavignac, D. Piccini, M. Unser, New parametric 3D snake for medical segmentation of structures with cylindrical topology, in Proceedings of the 2015 IEEE International Conference on Image Processing, Québec QC, Canada, September 27-30 (2015).
[27] G. Székely, A. Kelemen, C. Brechbhler, G. Gerig, Segmentation of 2D and 3D objects from MRI volume data using constrained elastic deformations of flexible Fourier contour and surface models, Medical Image Analysis 1(1) (1996), 19–24.
[28] P. Thévenaz, R. Delgado-Gonzalo, M. Unser, The ovuscule, IEEE Transactions on Pattern Analysis and Machine Intelligence 33(2) (2011), 382-393.
[29] G. Umlauf, Analyzing the characteristic map of triangular subdivision schemes, Constructive Approximation 16(1) (2000), 145-155.
[30] G. Umlauf, A technique for verifying the smoothness of subdivision schemes. In: Lucian, M.L., Neamtu, M. (eds.), Geometric Modeling and Computing, Nashboro Press, (2004), 513–521.
[31] D. Zorin, P. Schröder, W. Sweldens, Interpolating subdivision for meshes with arbitrary topology. In Proceedings of the 23rd International Conference on Computer Graphics and Interactive Techniques, (1996), 189–192.